JGR Earth Surface

RESEARCH ARTICLE
10.1029/2021JF006240

Near-Surface Geomechanical Properties and Weathering Characteristics Across a Tectonic and Climatic Gradient in the Central Nepal Himalaya

William G. Medwedeff[1], Marin K. Clark[1], Dimitrios Zekkos[2], A. Joshua West[3], and Deepak Chamlagain[4]

[1]Department of Earth and Environmental. Sciences, University of Michigan, Ann Arbor, MI, USA, [2]Department of Civil and Environmental Engineering, University of California at Berkeley, Berkeley, CA, USA, [3]Department of Earth Sciences, University of Southern California, Los Angeles, CA, USA, [4]Department of Geology, Tri-Chandra Multiple Campus, Tribhuvan University, Kathmandu, Nepal

Abstract Shallow bedrock strength controls both landslide hazard and the rate and form of erosion, yet regional patterns in near-surface mechanical properties are rarely known quantitatively due to the challenge in collecting *in situ* measurements. Here we present seismic and geomechanical characterizations of the shallow subsurface across the central Himalayan Range in Nepal. By pairing widely distributed 1D shear wave velocity surveys and engineering outcrop descriptions per the Geological Strength Index classification system, we evaluate landscape-scale patterns in near-surface mechanical characteristics and their relation to environmental factors known to affect rock strength. We find that shallow bedrock strength is more dependent on the degree of chemical and physical weathering, rather than the mineral and textural differences between the metamorphic lithologies found in the central Himalaya. Furthermore, weathering varies systematically with topography. Bedrock ridge top sites are highly weathered and have S-wave seismic velocities and shear strength characteristics that are more typical of soils, whereas sites near valley bottoms tend to be less weathered and characterized by high S-wave velocities and shear strength estimates typical of rock. Weathering on hillslopes is significantly more variable, resulting in S-wave velocities that range between the ridge and channel endmembers. We speculate that variability in the hillslope environment may be partly explained by the episodic nature of mass wasting, which clears away weathered material where landslide scars are recent. These results underscore the mechanical heterogeneity in the shallow subsurface and highlight the need to account for variable bedrock weathering when estimating strength parameters for regional landslide hazard analysis.

Plain Language Summary Rock strength controls the occurrence of landslides and the relationship between topography and erosion, but it is rarely known in natural environments because the most common measurement techniques are designed for individual site characterization and they are time-consuming to apply over broad spatial scales. In this paper, we apply a unique sampling strategy consisting of two field-based measurement techniques that are relatively portable and quick to apply repeatedly, and provide rock strength information over the scale of an outcrop (tens of meters). We apply our approach to an area of central Nepal where rock strength estimates are particularly important to know due to the high landslide hazard in this region. Our results show that rock strength is strongly controlled by the degree of weathering (i.e., the breakdown of rock by chemical and physical processes), which varies widely in Nepal depending on the local climate and topographic characteristics. In particular, we find that weathering is systematically greater (and thus rock strength is lower) on ridges compared to valley bottoms. On hillslopes between ridges and valleys, both weathering and rock strength are highly variable and difficult to predict, highlighting the need to further investigate regional variability in rock strength for future landslide hazard assessment.

Key Points:

- We employ seismic surveys and geomechanical rockmass characterizations to investigate regional patterns in rock strength
- No single variable explains the observed patterns in near-surface mechanical properties within this tectonically active terrain
- Weathering characteristics associated with ridge-to-channel topography contributes order-of-magnitude variations in near-surface strength

Supporting Information:

Supporting Information may be found in the online version of this article.

Correspondence to:

W. G. Medwedeff,
wmedwed@umich.edu

Citation:

Medwedeff, W. G., Clark, M. K., Zekkos, D., West, A. J., & Chamlagain, D. (2022). Near-surface geomechanical properties and weathering characteristics across a tectonic and climatic gradient in the Central Nepal Himalaya. *Journal of Geophysical Research: Earth Surface*, *127*, e2021JF006240. https://doi.org/10.1029/2021JF006240

Received 30 APR 2021
Accepted 21 DEC 2021

Author Contributions:

Conceptualization: William G. Medwedeff, Marin K. Clark, Dimitrios Zekkos
Data curation: William G. Medwedeff
Formal analysis: William G. Medwedeff
Funding acquisition: Marin K. Clark, Dimitrios Zekkos, A. Joshua West, Deepak Chamlagain
Investigation: William G. Medwedeff
Methodology: William G. Medwedeff, Marin K. Clark, Dimitrios Zekkos, A. Joshua West, Deepak Chamlagain

1. Introduction

The strength of rock and soil in the shallow subsurface is a fundamental control on the erosion of landforms and the pace of landscape evolution. Since the time of Gilbert (1877), it has been understood that stronger rocks are more resistant to erosion by frost cracking, landsliding, and abrasion by channel sediment, and modern studies have demonstrated these relationships quantitatively (Eppes et al., 2018; Sklar & Dietrich, 2001). This erosional resistance manifests in individual landforms as steep narrow canyons, river knick-points, and critically

Project Administration: Marin K. Clark, Dimitrios Zekkos, A. Joshua West, Deepak Chamlagain
Supervision: Marin K. Clark, Dimitrios Zekkos, A. Joshua West
Writing – original draft: William G. Medwedeff, Marin K. Clark
Writing – review & editing: William G. Medwedeff, Marin K. Clark, Dimitrios Zekkos, A. Joshua West, Deepak Chamlagain

stable hillslope gradients that are determined by the shear strength of the bedrock. At landscape scales, bedrock strength has been proposed as a factor controlling topographic relief (Montgomery & Brandon, 2002; Schmidt & Montgomery, 1995; Townsend et al., 2020), landslide frequency-magnitude statistics (Frattini & Crosta, 2013; Jeandet et al., 2019; Medwedeff et al., 2020), and autogenic river network reorganization (Forte et al., 2016; Gallen, 2018). While these qualitative connections between near-surface rock strength and landscape characteristics are well established, regional patterns and variability in rock strength are rarely known due to the effort involved in collecting *in situ* measurements at landscape scales. Field data is especially lacking in tectonically active landscapes, where steep terrain inhibits access, despite the fact that landslide hazard and rates of landscape evolution are highest in these regions.

Measuring rock strength over landscape scales is fundamentally challenging because of the heterogeneous nature of the shallow subsurface. Variations in bedrock lithology, bedrock fractures, and gradients in chemical weathering drive both lateral and vertical heterogeneity in mechanical characteristics, even at the scale of individual landforms (Anderson et al., 2007; Clarke & Burbank, 2010, 2011; Neely et al., 2019; Shobe et al., 2017). Furthermore, laboratory experiments show that the mechanical impact of weathering and fracturing in the shallow subsurface can lead to order-of-magnitude variations in the strength of otherwise compositionally similar rock (Hoek & Brown, 1997, 2019). Studies have also demonstrated an inverse relationship between rock strength and the sample size, owing to the greater opportunity for failure through the network of discontinuities in larger samples (Hoek & Brown, 1997). These effects challenge the common practice of using formation-level geologic units to characterize geotechnical properties and highlight the need to account for systematic patterns in chemical and physical bedrock weathering when estimating rock mass strength over regional scales.

While patterns in chemical and physical weathering partially depend on region-specific variables such as climate or susceptibility of bedrock minerology to chemical alteration, recent studies have increasingly highlighted a systematic increase in the vertical extent of weathering from valley bottoms to ridges (e.g., Riebe et al., 2017). Several mechanisms have been proposed to explain this pattern, but a common theme is the ease with which reactive meteoric fluids are able to infiltrate fracture networks in the subsurface. At the scale of tens to hundreds of meters, patterns in bedrock fractures are largely controlled by topographic stresses, leading to deeper and more severe weathering under ridges compared to valley bottoms (Miller & Dunne, 1996; Moon et al., 2017; Slim et al., 2015; St. Clair et al., 2015). A similar ridge-to-channel weathering gradient is predicted by reactive transport modeling where pore fluids below the water table are assumed to be in chemical equilibrium with the bedrock, which inhibits chemical alteration of bedrock in channels that meet the water table (Rempe & Dietrich, 2014). Superimposed on ridge-channel patterns, the aspect dependence of solar insolation and thermal cycles on the degree of bedrock fracturing by frost cracking leads to deeper fluid penetration and increased weathering on slopes receiving less sunlight (Anderson et al., 2013, 2014; Befus et al., 2011). Finally, accumulation of weak, weathered material also depends on the balance between local erosion rates and the rate of weathering front advance (Anderson et al., 2019; Dixon et al., 2012; Ferrier & Kirchner, 2008; Gu et al., 2020), potentially leading to enhanced variability in the thickness of the weathered zone on steep hillslopes where landslide erosion periodically clears away weathered bedrock (Gabet, 2007).

Although the weathering and fracturing mechanisms described above do account for some variability in near-surface bedrock strength, questions remain regarding the relative importance of each mechanism, and how this balance depends on environmental and geologic context that differs between landscapes. This knowledge gap partially reflects the tendency for previous studies to focus on individual mechanisms affecting chemical and physical weathering, often over relatively small spatial scales such as those cast by a single borehole or 2D seismic survey. While such focused investigations are necessary to understand bedrock weathering from a process standpoint, mechanical properties of the shallow subsurface often reflect a combination or competition of factors rather than the effects of one individual variable (Anderson et al., 2012; Riebe et al., 2017). The complexity of multiple interacting controls on rock strength is likely to be pronounced in tectonically active landscapes, which are often characterized by a variety of rock types and gradients in climate and topography. A large number of geotechnical measurements are therefore needed to adequately evaluate the factors that most-strongly control rock strength over regional scales, and to constrain the level of natural variability that should be expected even after the systematic trends in rock mass properties have been accounted for.

In this paper, we employ a novel strategy using field-based engineering approaches that are inexpensive and portable, and therefore feasible to apply at the scale needed to collect regional data. We investigate both the

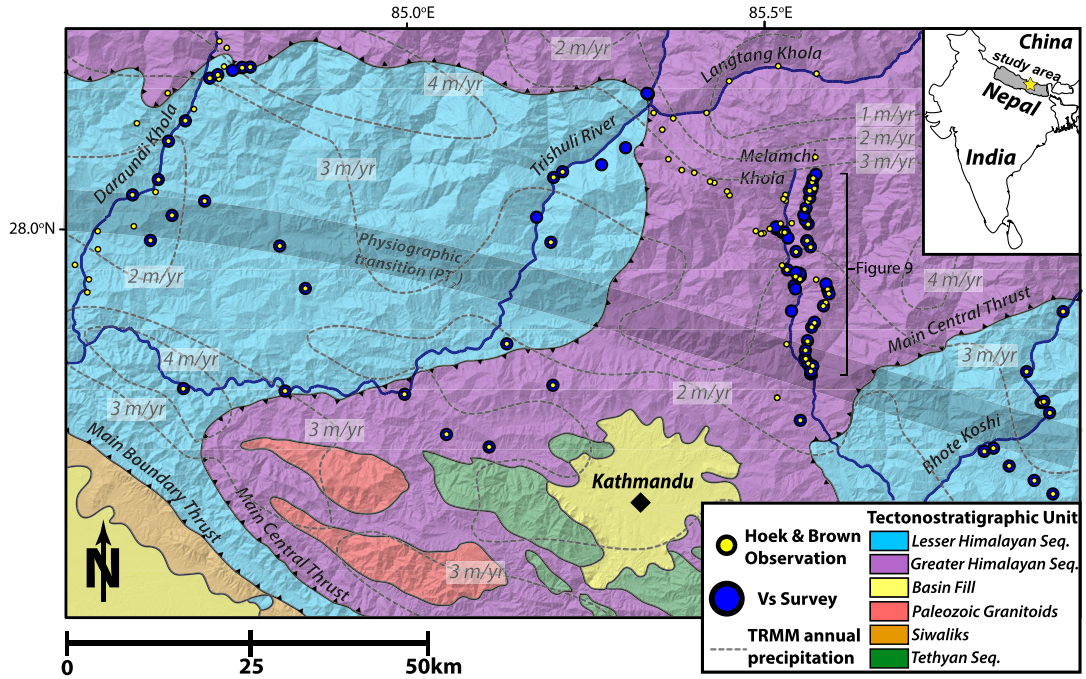

Figure 1. Simplified geology and structure of the Central Nepal Himalaya modified from Shrestha and Shrestha (1986). Circles denote field surveys for geological strength index (yellow, $n = 108$) and seismic velocities (blue, $n = 85$). These data were collected in 2017 and 2018, after the M_w7.8 Gorkha earthquake. TRMM derived mean annual precipitation highlights the climatic variability in the Himalaya with a strong association with mean topography (Bookhagen & Burbank, 2010). The "physiographic transition" denotes an abrupt increase in erosion rates, topographic slope and elevation north of this boundary (Hodges et al., 2001).

surface and subsurface mechanical characteristics by combining active seismic surveys and outcrop-scale engineering field descriptions. Where outcrops are exposed at the surface, we apply the geological strength index (GSI) classification system to quantify the degree of chemical and physical weathering in the rockmass (Hoek & Brown, 1997), which is then used to predict bedrock shear strength at depth. These predictions are compared to direct measurements of material properties using 1D shear wave velocity (V_s) surveys. We apply these techniques over a ~200 km by 50 km swath of the Himalayan Range front in Central Nepal across gradients in climate and topography (Figure 1).

2. Study Area and Sampling Strategy

The Himalayan Mountains are characterized by some of the highest erosion rates and greatest landslide hazard on Earth (Marc et al., 2019). Here, patterns in near-surface strength and erodibility contribute to hazard mitigation and understanding geomorphic processes but are insufficiently known at regional scales. Our investigation covers a portion of the central Nepalese Himalaya affected by the 2015 M_w7.8 Gorkha Earthquake, which triggered over 24,000 landslides (Roback et al., 2018). In addition to the importance of regional strength estimates for future landslide hazard analysis, this part of central Nepal also offers the opportunity to evaluate how patterns in near-surface properties vary with respect to gradients in climate and topography, with the ultimate goal of an improved, processes-based understanding of the geologic and environmental factors that control near-surface strength.

2.1. Geologic Background

The Himalayan range is broadly characterized by a series of north-dipping, crustal-scale thrust faults, making up the southern margin of the Indo-Asian convergent plate boundary (e.g., Gansser, 1964; Le Fort, 1975; Shelling & Arita, 1991, Figure 1). The structurally oldest and most northerly fault is the Main Central Thrust (MCT), with the Main Boundary Thrust (MBT) and Main Frontal Thrust (MFT) occupying younger and more southerly

positions respectively. The MCT and MBT are surface features, which merge at depth into the plate boundary décollement, the Main Himalayan Thrust (MHT). The MFT defines the surface expression of the MHT at the southern edge of the Siwaliks rock sequence. The majority of the total shortening rate across the Himalaya (around 20 mm/yr) is accommodated on the seismically active MHT (Bilham et al., 1997; Grandin et al., 2012). Tectonic activity of the thrust belt has contributed to mean elevation of ∼5 km with the rise of mountain peaks above 8 km and deep river gorges with 2–3 km of relief, with lower and higher elevation regions separated by a "physiographic transition" (PT_2, Hodges et al., 2001). The Himalayan range front and Tibetan Plateau together exert a strong orographic effect on both mesoscale precipitation and global atmospheric circulation, leading to peak rainfall intensity during the summer monsoon season and an orographic gradient in precipitation that roughly follows the physiographic transition (increasing from ∼2 to over 4 m/yr) and a concentration of precipitation south of the Kathmandu Basin in the Marabhat Range (over 3 m/yr) (Figure 1; Shrestha et al., 2012; Bookhagen & Burbank, 2010). The elevation and precipitation gradient across the PT_2 gives rise to a range of local climatic zones and ecosystems (Schickhoff, 2005). The majority of our field sites are within a few tens of kilometers of this boundary.

Rock sequences in Central Nepal include the Lesser and Greater Himalayan Series (major tectonostratigraphic units), which are recognized throughout the Himalayan orogen and are separated by the MCT (Gansser, 1964, Figure 1). Although there is generally an association between the Greater Himalaya Series (GH) rock exposure and the higher elevations of the Himalaya, in our study area the GH Series is also exposed farther south at lower elevation compared to equivalent latitudes along strike of the range due to the Kathmandu Nappe (Figure 1). The Lesser Himalayan (LH) Series contains metasedimentary slates, chloritic and sericitic phyllites, and pelitic schists (DeCelles et al., 2001). The GH series contains a sequence of high-grade metasedimentary rocks buried to lower crustal pressure-temperature conditions (Macfarlane, 1993) and is predominantly composed of kyanite-to sillimanite-grade pelitic schists, augen gneisses, and migmatites in central Nepal (Parrish & Hodges, 1996). Calc-silicate gneisses, amphibolites, and orthogneisses are also found in the area but are less prevalent (Parrish & Hodges, 1996).

2.2. Sampling Strategy

Our sampling strategy balanced a distributed regional survey with focused investigations of the environmental factors likely to control near-surface mechanical properties. Of these potential controlling factors, we prioritized sampling across gradients in precipitation, the different metamorphic rock units that characterize the bedrock, and several metrics of topography (i.e., elevation, slope, aspect, and topographic position). Fieldwork was carried out in 2017 and 2018 after the M_w7.8 Gorkha Earthquake.

We primarily targeted sites where the native subsurface material was exposed with thin-to-absent mobile soil cover ($n = 68$). We refer to these sites throughout the manuscript as "bedrock sites" to distinguish them from mobile material, although we note that in some cases the bedrock was highly weathered (i.e., saprolite). Additionally, 17 V_s surveys were collected on colluvial material. Dense vegetation and steep topography often required the use of unpaved roads and trails for access to bedrock exposures and to reasonably deploy ∼40–50 m of linear seismic arrays, which typically yielded a 20–30 m depth of investigation. The majority of our bedrock sites are concentrated in the LH Ranimatta Formation ($n = 22$ V_s sites and 27 GSI observations) and the GH Himal Group ($n = 33$ V_s sites and 69 GSI observations). The Ranimatta Formation is characterized by chloritic and muscovite phyllites, as well as muscovite schists. The Himal Group bedrock sites are primarily characterized by garnet mica schists, garnet biotite gneisses, augen gneisses, as well as migmatites and amphibolite-bearing gneisses at high elevations in the Melamchi and Langtang watersheds. Although slates are common in some parts of the LH series (DeCelles et al., 2001), they are relatively sparse within our area of investigation and we only surveyed slate bedrock at two of our V_s sites in the Galyang Formation.

We targeted a roughly equal number of sites on ridges, hillslopes, and near channel bottoms to evaluate differences in properties associated with ridge-channel topography position. We classify sites as "ridges" only if they lie directly on the ridge crest with divergent flow in all directions, and we require that channel sites are within 20 m vertically and 100 m horizontally of a bedrock channel (the channel bed itself is usually underwater). All remaining sites are classified as hillslope sites. Three sampling transects along first-order drainage divides bounding the Daraundi, Melamchi, and Bhote Koshi watersheds were targeted for gradients of precipitation, elevation, slope and aspect (Figure 1). These transects span elevations from 1 to 4 km above sea level, extend from subtropical to

alpine environments across a range of mean annual precipitation from 1 to 4 m/yr, and vary in mean slope from ~20° to 40°.

3. Methods

Shallow seismic surveys and rock mass observations from outcrops are complementary techniques that fully characterize the near surface environment in terms of both quantifying shear strength and relating surface measurements to depth. Specifically, we combine 1D active seismic surveys and engineering characterization using the GSI classification system (Hoek & Brown, 1997, 2019). Seismic surveys were analyzed for shear wave velocity, which depends on the stiffness of rock and soil in the shallow subsurface. The GSI classification characterizes the bulk mechanical properties of rock outcrop exposures, where the intact strength of the rock mass is penalized based on the structure and density of discontinuities (such as fractures, bedding planes and foliation) and the weathered condition of the discontinuity surfaces. The advantage of the GSI classification system lies in ease of collection, requiring only field observations of exposed outcrops. Empirical relationships have also been developed that permit estimation of shear strength values based on GSI observational data, and such quantification is a distinct advantage over other rank classification systems (e.g., Selby, 1980). GSI observations are based on surface observations, while the seismic surveys offer a view into the subsurface and cast a larger spatial scale (~40 m array), thus reducing the impact of meter scale variability in elastic properties that may not be representative of the macroscopic behavior of the rock mass. In total, we collected 88 active seismic surveys at a total of 85 unique sites and made 111 outcrop observations of GSI at 108 unique sites. We collected both sets of data at 54 sites where bedrock was exposed adjacent to our seismic survey sites (Figure 1).

3.1. Shallow Seismic Surface Wave Techniques

V_s is related to the low-strain shear modulus, G_{max}, such that $G_{max} = \rho V_s^2$ where ρ is the material density (Shearer, 2009). V_s is thus a direct measure of the stiffness of rock and soil, and is broadly correlated to shear strength as stiffer ground materials tend also to be stronger. V_s30, or the time-averaged shear-wave velocity over the top 30 m of the subsurface, is a standard metric in geotechnical earthquake engineering used to assess seismic site response and ground failure potential. Compared to the compression wave velocity (V_p), V_s also offers the advantage of a low sensitivity to the location of the groundwater table.

While it is possible to measure shear-wave body phases directly, they attenuate faster than surface waves and require horizontal-component geophones which are expensive and more time consuming to install (Park et al., 1999a; Pasquet & Bodet, 2017). The vast majority of near-surface practitioners instead opt to infer V_s by inversion of surface wave measurements, and in particular Rayleigh waves. From elastic wave propagation theory, Rayleigh waves travel near 90% of the V_s and decay in amplitude exponentially with depth (Shearer, 2009). The depth of penetration of surface waves is a function of wavelength, with lower frequency waves inducing particle motion deeper in the profile where the stiffness, and thus V_s, of earth materials tends to be higher. As a result, surface waves of different frequencies travel at different phase velocities (i.e., wave dispersion). A soil/rock column with a steeper gradient in V_s with depth yields a greater dispersion of Rayleigh wave phase velocities, making it possible to infer the V_s profile by inversion of the Rayleigh wave dispersion curve (e.g., as shown in Figure 2). Resolution is highest near the surface and progressively decreases with depth because increasingly lower-frequency waves are used to sample deeper regions, resulting in increased averaging of the subsurface in deeper parts of each profile (Stokoe & Santamarina, 2000).

3.1.1. Equipment and Field Acquisition

Seismic data were collected with Geometrics ES300 and Geode seismographs using 4.5 Hz vertical component geophones laid out in a linear array (Figure 2a). A 4.5 kg (10 lb) sledgehammer was struck against a 5 cm thick plastic plate to generate the stress waves. We used either 16 or 24 channel seismic arrays (30 and 58 surveys with each setup, respectively), and between 0.30 and 3.05 m (1–10 ft) spacing between geophones depending on the space available at each site and the target depth of investigation. For a fixed number of channels, array length presents a trade-off between the depth of investigation and the detail in velocity structure resolved near the surface. For the majority of our surveys, we maximized array length to the space available (typically ~40 m), allowing for a depth of investigation of approximately 20 m or deeper. At three sites we conducted multiple surveys with different receiver spacing to enhance both depth of investigation and resolution near the surface. We used a near

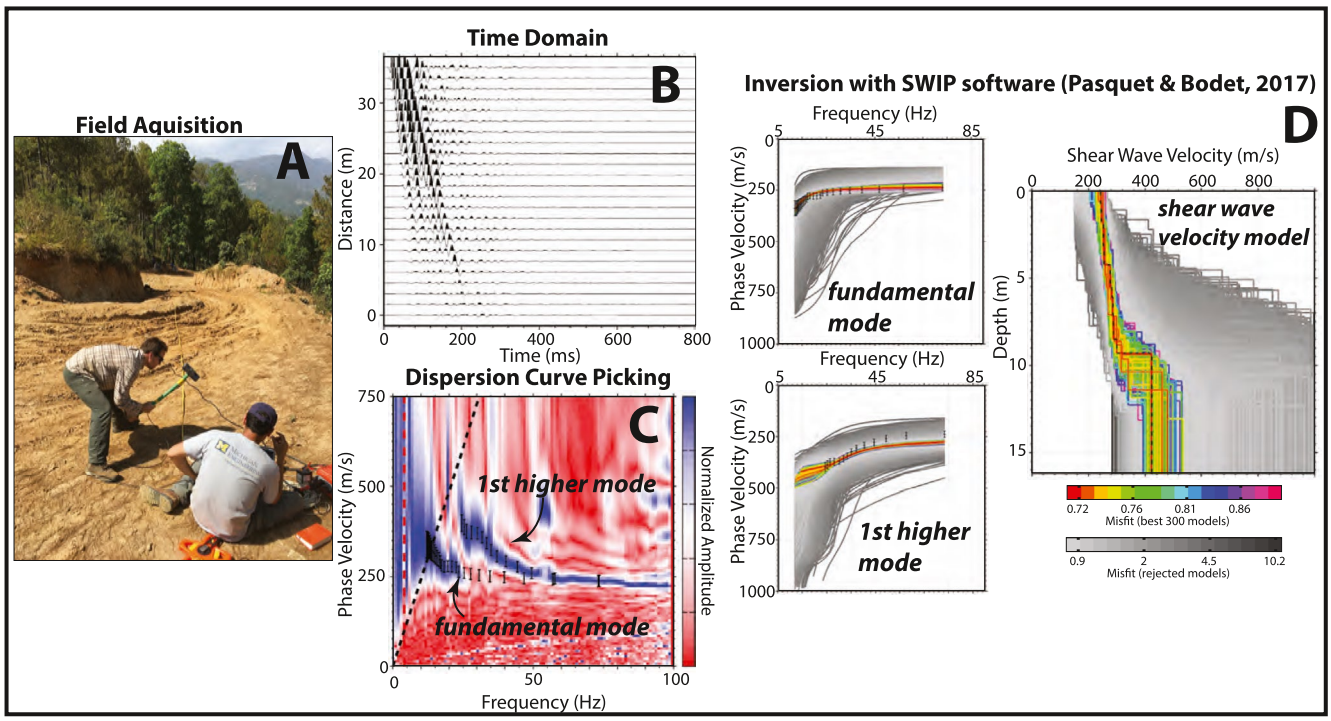

Figure 2. Example data collection, surface wave dispersion interpretation, and inversion of dispersion for a 1D V_s profile. (a) Acquisition of seismic data at a typical site using a sledgehammer source. (b) Raw seismic data showing a 24-channel survey, made with eight stacked shot gathers. (c) The dispersion image corresponding to the data in (b). The dispersion image was interpreted to show two propagation modes, as indicated with the black points with uncertainty bars. The dashed black line indicates a constant wavelength equal to the length of the seismic array, which we use as a geometrical limit for our dispersion picks. (d) Inversion of the surface wave propagation modes picked in (c). The Monte Carlo inversion scheme explores candidate V_s models that match the manually picked dispersion profile.

offset, that is, the distance between sledgehammer source and the first geophone, of 15%–20% of the total array length to avoid near-field effects (Park et al., 1999a; Yoon & Rix, 2009). All surveys stacked 8 sledgehammer shots to improve the signal-to-noise ratio.

3.1.2. Multichannel Analysis of Surface Waves

The multichannel analysis of surface waves (MASWs) technique utilizes wavefield transformation of stacked shot records to improve the coherency of Rayleigh wave modes from noise, which often adversely influences interpretation of dispersive wavefields (Park et al., 1999a). Wavefield transformation produces a dispersion image where the dominant Rayleigh wave modes appear as high-amplitude regions of the plot (Figure 2). Dispersion curves for fundamental and higher modes are interpreted manually along coherent patterns of energy maxima. While there are theoretically an infinite number of propagation modes (analogous to harmonics on a string), the energy partitioned into each mode depends on the velocity structure of the site (Park et al., 1999b; O'Neill & Matsuoka, 2005). Sites with particularly high velocity gradients, exceptionally stiff layers, or velocity reversals are more likely to produce dominant higher modes (Park et al., 1999b; O'Neill & Matsuoka, 2005). We analyzed dispersion curves and performed inversions for V_s using the open-source package Surface Wave Inversion and Profiling (SWIP) (Pasquet & Bodet, 2017). We identified maxima for higher modes at 59 of our 85 unique sites and picked up to a maximum of four modes in individual records. For sites where we collected multiple surveys with different receiver spacing ($n = 3$), we picked each dispersion curve separately and combined the picks for the inversion (see data repository).

Inversion of surface wave dispersion curves for S-wave velocity profiles provides a non-unique solution, as multiple S-wave velocity profiles may produce similar theoretical dispersion curves (Foti et al., 2009). A key feature of the SWIP scheme is the probabilistic distribution of posterior models, which indicate the non-uniqueness of the solution by the degree to which the V_s structure is constrained by the dispersion curve picks. Using a Voronoi-cell-based Monte Carlo inversion scheme, inversions explore candidate velocity models whose synthetic dispersion curves match the manual picks (Figure 2c). Misfit is computed in the phase velocity–frequency domain,

and the inversion accounts for up to five modes. Although all modes are weighted equally in the inversion process, lower frequencies (where the fundamental mode generally dominates) are given more weight because SWIP interpolates the user's dispersion picks linearly in terms of wavelength. This strategy permits greater misfit for thin layers toward the surface in exchange for a more robust representation of the bulk properties of the site (Pasquet & Bodet, 2017). We found that the most significant parameter affecting the inversion process was the decision to allow velocity reversals versus forcing a monotonic increase in velocity with depth. We therefore ran two inversions for each site, both permitting and prohibiting velocity reversals. We chose the model with velocity inversions only if it (a) resulted in a lower misfit than the monotonic model, and (b) also converged to a solution with realistically sized velocity jumps. Under these criteria our favored models contain velocity inversions in 5 of 85 unique sites (see details in Supplementary Material). Although we recognize that a definitive assessment of the V_s profile with depth is not possible, especially for complex site conditions, we note that it has been shown before that the final S-wave velocity profile and specific location of low-velocity layers (which may be inaccurate) has little effect on average velocity of each site (Garofalo et al., 2016).

3.1.3. Estimation of V_s30

V_s30, or the time-averaged shear-wave velocity in the top 30 m of the subsurface, is a standard metric in geotechnical earthquake engineering used to quantify seismic site response and ground stiffness. While it is therefore desirable to report V_s30 as a standard point of reference, few of our V_s surveys resolved depths of investigation beyond 20 m. Here we apply an extrapolation following the approach of Wang and Wang (2015), as in Equation 1.

$$\log V_s(30) = \log V_s(z_2) + \frac{\log 30 - \log z_2}{\log z_2 - \log z_1}\left[\log V_s(z_2) - \log V_s(z_1)\right] \quad (1)$$

where $V_s(z_1)$ and $V_s(z_2)$ are the time-averaged shear-wave velocities to depths z_1 and z_2, respectively. Equation 1 assumes that V_s has a log-linear dependence on the increasing confining stress with depth. Compared to purely empirical regressions, the Wang and Wang (2015) approach is not regionally dependent and does not require extensive measurements to derive empirical coefficients, while still maintaining 96% accuracy in site classifications compared to direct V_s30 observations (Wang & Wang, 2015). We use $z_1 = 10$ m and $z_2 =$ the maximum depth of each survey to compute V_s30 estimates for each survey.

3.2. Hoek and Brown Rockmass Characterizations

The GSI and the Hoek and Brown criterion together provide a rockmass strength envelope under a range of stress conditions, which we exploit to extrapolate shear strength estimates to 20 m depth using an assumption of lithostatic stress conditions.

3.2.1. Field Estimation of Geological Strength Index

The GSI classification chart is based on the rock mass structure (pervasiveness, interlocking, and density of fractures) and weathering and roughness characteristics of discontinuity surfaces (Figure 3). For each outcrop, we recorded observations that relate to a range of values for GSI. For example, we described the outcrop shown in Figure 3a as: "Garnet mica schist. Three primary discontinuity sets, perpendicular, spaced ~10–30 cm. Two discontinuity sets are well-defined, with one of them parallel to mineral foliation. Platy micas create flaky structure at a fine scale. Weathering moderate and penetrates outcrop thoroughly. Intact pieces are easily split along discontinuities with a hammer blow." From the GSI chart (Figure 3b), three intersecting discontinuity sets relate to a "blocky" structure. The moderately weathered surfaces relate to "fair" surface quality conditions. Together, these ratings result in a GSI estimate of 50–65.

In addition to GSI, the Hoek and Brown criterion relies on an estimate of the uniaxial compressive strength of intact blocks (UCS_{intact}, i.e., in the absence of fractures). We estimated this parameter based on the table provided by Hoek and Brown (1997), which relates a range of UCS_{intact} values to qualitative tests that are easily carried out in the field (for example, the approximate number of hammer blows required to break a hand specimen or the sound created by a hammer strike to intact rock).

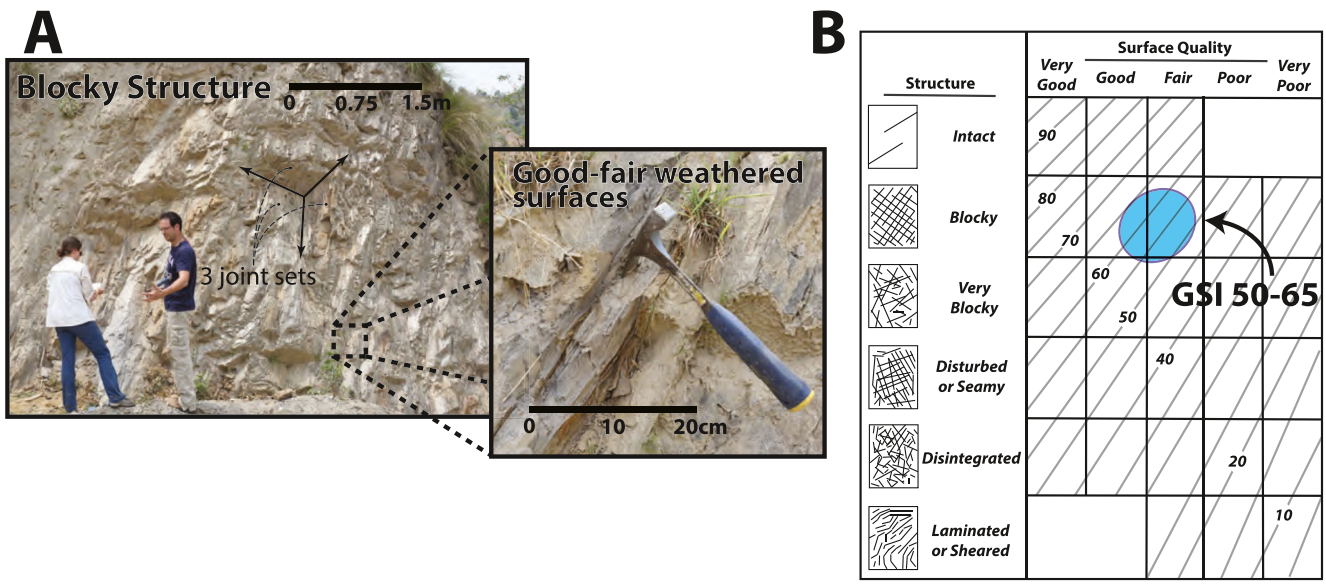

Figure 3. Example characterization of rockmass properties with the Geological Strength Index (GSI) rating system. Outcrops are classified based on the pervasiveness, interlocking, and density of fractures ["structure" axis in (b)], as well as the weathering conditions and roughness of the discontinuities ["surface quality" axis in (b)]. The resulting GSI estimate may then be used as an input parameter into the Hoek and Brown strength criterion, thus providing a method to estimate rock strength quantitatively based on qualitative field observations.

3.2.2. Integration of GSI Into Hoek and Brown Criterion and Estimation of Shear Strength Profiles

Predicted shear strength profiles are derived from the generalized Hoek and Brown criterion (Figure 4). The principal stresses at failure are given by:

$$\sigma_1' = \sigma_3' + \sigma_{ci}\left(m_b\frac{\sigma_3'}{\sigma_{ci}} + s\right)^a \tag{2}$$

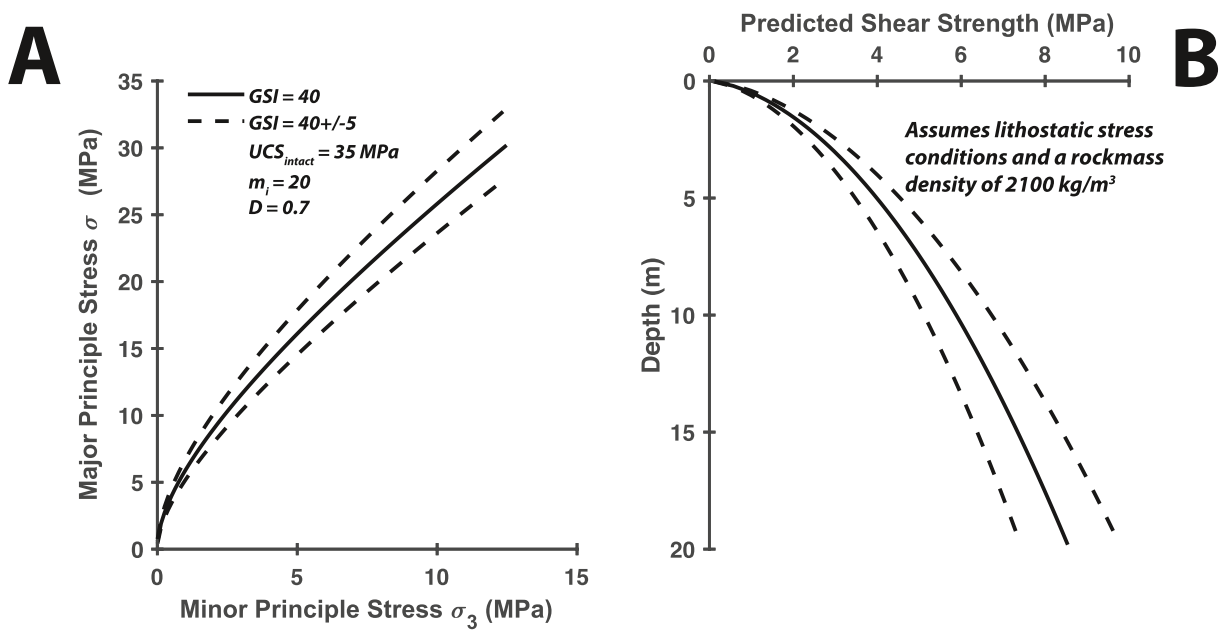

Figure 4. Estimation of shear strength profiles using geological strength index (GSI) observations and the Hoek and Brown criterion. (a) Example predicted strength envelope for GSI = 40 ± 5, UCS_{intact} = 35 MPa, and Hoek and Brown parameters $m_i = 20$ and $D = 0.7$. (b) The same strength envelope as in **A** but transformed to shear and normal stress components with the added assumption that the minimum principal stress at failure is given by $\sigma_3 = K_0\sigma_{lithostatic}$, where K_0 determines the magnitude of the stress exerted by the material in the horizontal direction. This analysis extends our surface outcrop observations into estimates of shear strength at depth.

where σ_{ci} is the UCS_{intact} and m_b is given by:

$$m_b = m_i \left(\frac{GSI - 100}{28 - 14D} \right) \tag{3}$$

s and a are constants given by:

$$s = exp \left(\frac{GSI - 100}{9 - 3D} \right) \tag{4}$$

$$a = \frac{1}{2} + \frac{1}{6} \left(e^{-GSI/15} - e^{-20/3} \right) \tag{5}$$

Finally, the factors m_i and D are empirical factors which depend on rock type and mechanical disturbance, respectively. For all of our sites we used values of 20 and 0.7 for m_i and D, respectively, which represent typical values for metamorphic rocks and disturbance induced by stress relaxation as rocks are mostly exposed at road cuts (Hoek & Brown, 1997, 2019). By using uniform values, we assume the range in lithology and mechanical disturbance is relatively small among our outcrop observations. Bedrock throughout the study area is characterized by crystalline metamorphic lithologies, and exposures range from natural outcrops to mechanically excavated road cuts (we observed no evidence of blast damage in any of the road cut observations).

To estimate shear strength profiles from the Hoek and Brown relationship, we recast the principal stresses into shear and normal components following Hoek et al., (2002), assuming a lithostatic stress field in dry conditions with an overburden density of 21 kN/m^3 (Figure 4b). We assume the minimum principal stress at failure is given by $\sigma_3 = K_0 \sigma_{lithostatic}$, where K_0 is the lateral earth pressure coefficient, which determines the magnitude of the pressure exerted by the material in the horizontal direction. K_0 typically varies between 0.7 for soft soils to 0.1 for intact rockmass with high frictional strength (Jaky, 1944; Mayne & Kulhawy, 1982). Here we adopt an intermediate value of $K_0 = 0.3$. We note that our shear strength predictions assume that the rockmass density, GSI and UCS_{intact} values estimated at the surface remain constant throughout the profile with depth. This assumption is clearly not always valid since the degree of weathering and fracturing is generally expected to decrease with depth in the near-surface, which would result in higher shear strength values at depth than predicted here.

4. Results

A wide range of mechanical characteristics associated with soil to rock are captured by the sites we surveyed, even for the "bedrock" only sites (Figure 5). The GSI observations also nearly encompass the full range of conceivable values, ranging from 0 to 95, with a mean value of 50 and a standard deviation of 21. The large range in GSI values results in shear strength estimates that range from 0.2 to 8.5 MPa at 5 m depth, characteristic of materials ranging from stiff soils to minimally fractured hard rock (Heimsath & Whipple, 2019; Sutcliffe et al., 2004). Although not surprising, we note that fractured and disturbed rock masses generally also have lower surface quality ratings (Figure 5a). The V_s data also span a large range from 140 to 1,500 m/s at the surface, to between 200 and 3,000 m/s at 20 m depth. Where the rock mass is classified as highly weathered according to the "surface quality" component of the GSI classification (warmer colors in Figure 5), we observe lower velocities that are characteristic of soil rather than rock [V_s30 between 180 and 360 m/s, Federal Emergency Management Agency (FEMA), 2004)], while less weathered sites (cooler colors) have V_s typical of unweathered rock (>760 m/s V_s30, FEMA, 2004). While our use of the "surface quality" measurement as a proxy for the degree of weathering inherently leads to a correlation with the shear strength profiles (which are based on GSI observations), we note that our weathering observations are independent of the V_s data.

The coefficient of variation (COV) provides a useful metric to assess how different physical factors influence rockmass properties. Grouping the V_s and GSI data by lithologic and geomorphic variables results in significantly lower COV for several of the categories compared with the COV for the undivided data set (Table 1, bold values indicate greater than 15% reduction in COV). The most systematic pattern is an increase in both average V_s and GSI from ridges, to hillslopes, to channel sites, with COV values for the ridge and channel sites that are especially low compared to those for the undivided data set. Elevations above tree line (~3.9 km in the Himalaya; Schickhoff, 2005) and slopes steeper than 35° are also associated with increased mean V_s and GSI, and lower COV values, which is consistent with previous studies that have argued for a threshold shift to kinetically limited

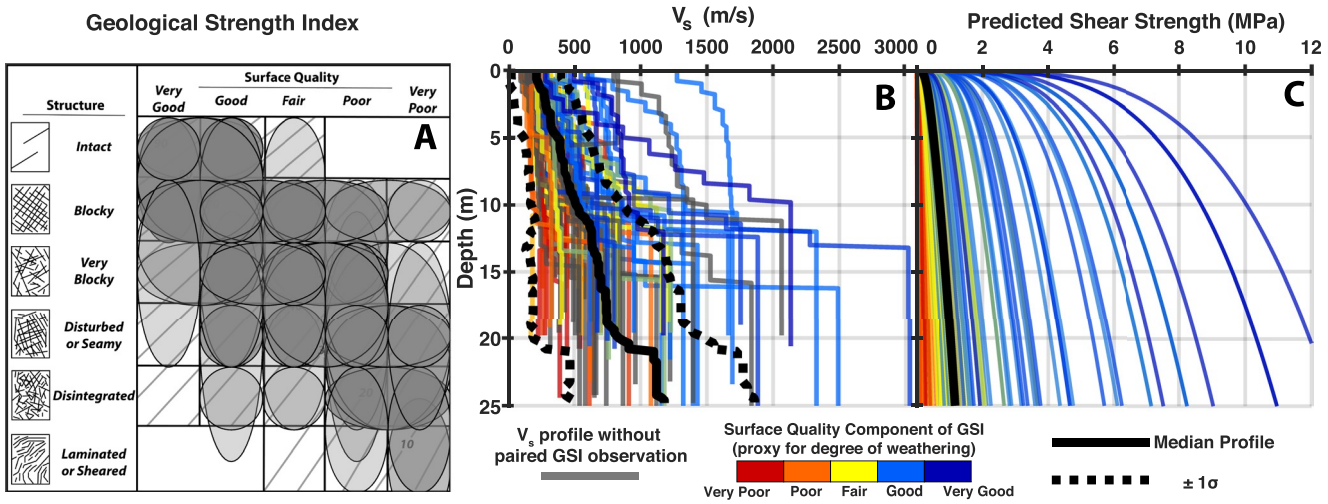

Figure 5. Measured geomechanical properties for all sites. (a) All outcrop geological strength index (GSI) observations for bedrock sites (n = 111; 108 unique sites). Transparent gray ovals correspond to the range of structural and weathering conditions observed at each outcrop, with darker shades of gray indicating overlapping measurements. (b) All active seismic surveys (n = 88; 85 unique sites), including 68 on weathered bedrock without soil cover, and 17 on colluvial mantle where bedrock likely lies beyond the depth of investigation. Color (blue to red) indicates the weathering component of the GSI observation (i.e., "surface quality") for the V_s surveys where bedrock was exposed; lines are colored gray if no outcrop existed at the site. Note that there are no corresponding GSI measurements for the colluvium sites. (c) The Hoek-Brown shear strength profiles predicted by the GSI values in (a) and the assumptions in Section 3.2.2. Blue to red colors relate to the weathering component of the GSI observation.

Table 1
Summary Statistics for All GSI and V_s Data

	GSI[a]	COV[b]	$V_{s\ 30}$[a]	COV[b]	$V_{s\ 20}$[a]	COV[b]	Depth to V_s = 500 m/s[a]
	Out of 100		m/s		m/s		m
All bedrock data	50 ± 21 n = 111	0.42	611 ± 342 n = 68	0.56	545 ± 300 n = 68	0.55	6.6 ± 4.5
Slate	53 ± 9 n = 3	**0.17**	636 ± 175 n = 2	**0.28**	556 ± 183 n = 2	**0.33**	5.6 ± 5.7
Phyllite	48 ± 19 n = 10	0.40	987 ± 379 n = 4	**0.39**	841 ± 263 n = 4	**0.31**	2.1 ± 2.7
Schist	46 ± 17 n = 54	0.38	571 ± 290 n = a7	0.51	502 ± 243 n = 37	0.48	7.3 ± 4.5
Gneiss	56 ± 26 n = 40	0.47	565 ± 334 n = 22	0.59	519 ± 331 n = 22	0.64	6.5 ± 4.2
Colluvium[c]	–	–	465 ± 95 n = 17	**0.21**	398 ± 84 n = 17	**0.21**	9.5 ± 3.3
Ridges	39 ± 21 n = 34	0.55	372 ± 133 n = 26	**0.36**	326 ± 101 n = 26	**0.31**	9.8 ± 2.4
Hillslopes	50 ± 19 n = 50	0.39	701 ± 328 n = 32	**0.47**	638 ± 303 n = 32	0.48	5.9 ± 4.8
Channels	65 ± 15 n = 27	**0.22**	956 ± 346 n = 10	**0.36**	788 ± 289 n = 10	**0.37**	3.7 ± 3.8
Elev. > 3.9 km	66 ± 14 n = 12	**0.22**	725 ± 210 n = 5	**0.29**	598 ± 170 n = 5	**0.28**	5.2 ± 3.4
Elev. < 3.9 km	49 ± 21 n = 104	0.43	602 ± 349 n = 63	0.58	540 ± 309 n = 63	0.57	6.7 ± 4.7
Slopes >35°	62 ± 14 n = 21	**0.22**	809 ± 373 n = 12	**0.46**	677 ± 307 n = 12	**0.45**	4.6 ± 4.4
Slopes <35°	48 ± 22 n = 95	0.45	568 ± 321 n = 56	0.57	513 ± 292 n = 56	0.57	7.1 ± 4.5
Southern aspect >120° & <250°	46 ± 22 n = 67	0.47	620 ± 298 n = 40	0.48	548 ± 276 n = 40	0.50	6.7 ± 4.3
All other aspects	56 ± 19 n = 49	**0.34**	599 ± 400 n = 28	0.67	541 ± 338 n = 28	0.62	6.3 ± 5.2
Mean annual precipitation >2.5 m/yr[d]	54 ± 21 n = 61	0.39	648 ± 344 n = 37	0.53	539 ± 283 n = 37	0.52	7.0 ± 4.4
Mean annual precipitation <2.5 m/yr	45 ± 20 n = 50	0.45	566 ± 337 n = 31	0.60	554 ± 331 n = 31	0.60	5.9 ± 4.7

[a]mean value, ± indicates 1σ. [b]Coefficient of variation (std/mean). Bold values indicate greater than 15% reduction in COV compared to entire data set. [c]Colluvium sites have been removed for statistics in all other categories. [d]Precipitation estimates based on calibrated TRMM product by Bookhagen & Burbank (2010).

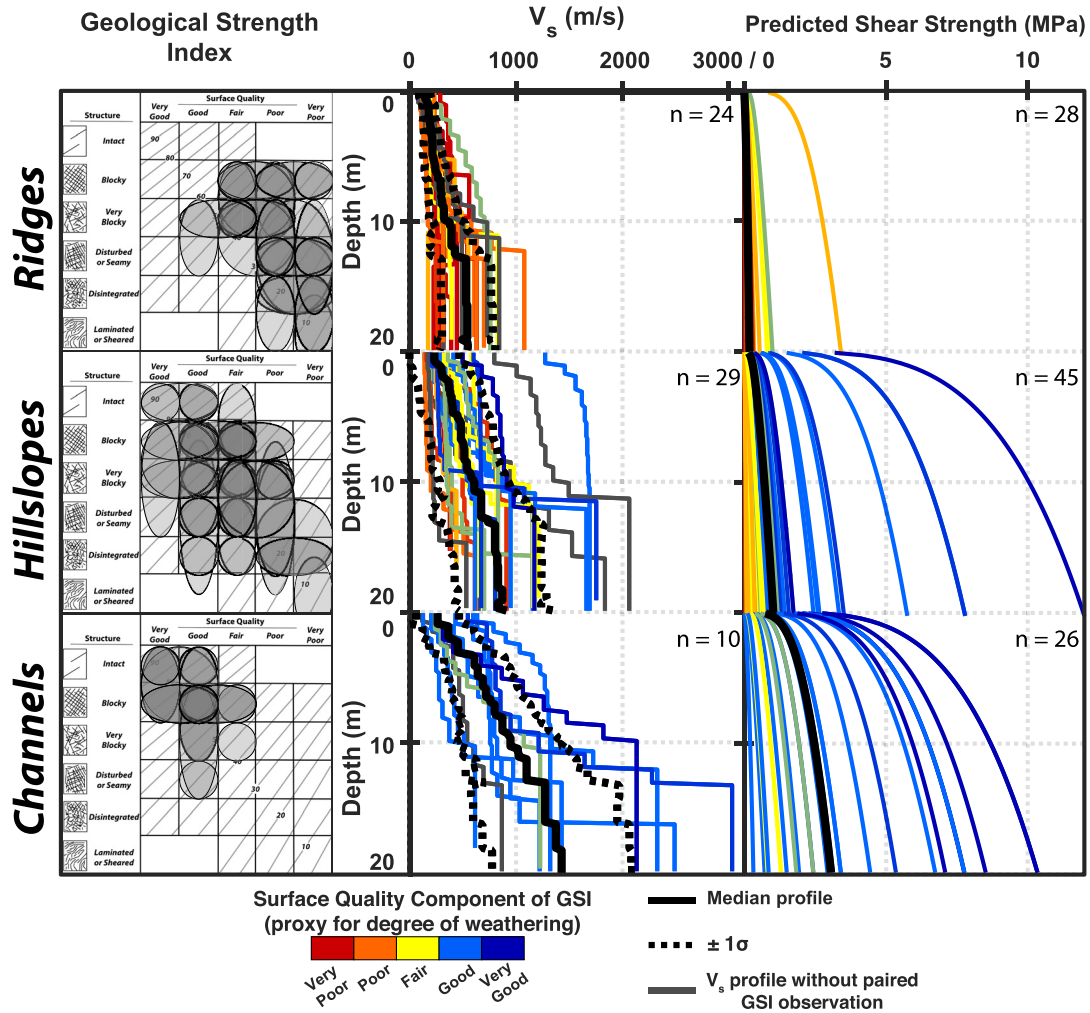

Figure 6. Geological strength index, V_s, and predicted shear strength profiles for sites on ridges, hillslopes, and near bedrock channels. Sites above tree line elevations (~3,900 m) are excluded.

weathering above alpine elevations and on steep slopes (Dixon et al., 2012; Riebe et al., 2004). Subdividing the data by metamorphic grade does not reveal any systematic trends, although we note that mean V_s is significantly higher in phyllites than in slates, schist, or gneisses. Finally, categorical divisions based on slope aspect and local annual precipitation produce relatively small differences in mean V_s and GSI, which do not clearly stand out against the level of variability within each category.

4.1. Variations in Bedrock Characteristics of Ridge to Channel Topography

We observe a systematic increase in mechanical competence from ridges to hillslopes to channels, which is driven by weathering conditions (Figure 6; Table 1). Excluding sites above tree line elevations (3.9 km; Schickhoff, 2005) because of the abrupt change in weathering and vegetation associated with high altitudes unrelated to the topography itself (Riebe et al., 2004), no ridge sites have weathering observations exceeding "fair" conditions (mean GSI = 32 ± 16), and the median ridge V_s profile and predicted shear strength values are typical of highly weathered rock and saprolite (~180 m/s and 0.01 MPa at the surface to 500 m/s and 0.2 MPa at 20 m depth; FEMA, 2004; Heimsath & Whipple, 2019; Sutcliffe et al., 2004). Weathering conditions among hillslope sites span the full range from "very poor" to "very good" (mean GSI = 48 ± 19) with the median V_s profile ranging from 280 to 800 m/s from the surface to 20 m depth, and shear strength values of 0.2–1.0 MPa from the surface to 20 m depth. GSI observations at channel sites are higher and more consistent (mean GSI = 67 ± 14), with only one site having a surface weathering value lower than "fair." Channel V_s profiles are typical of fresh rock, with

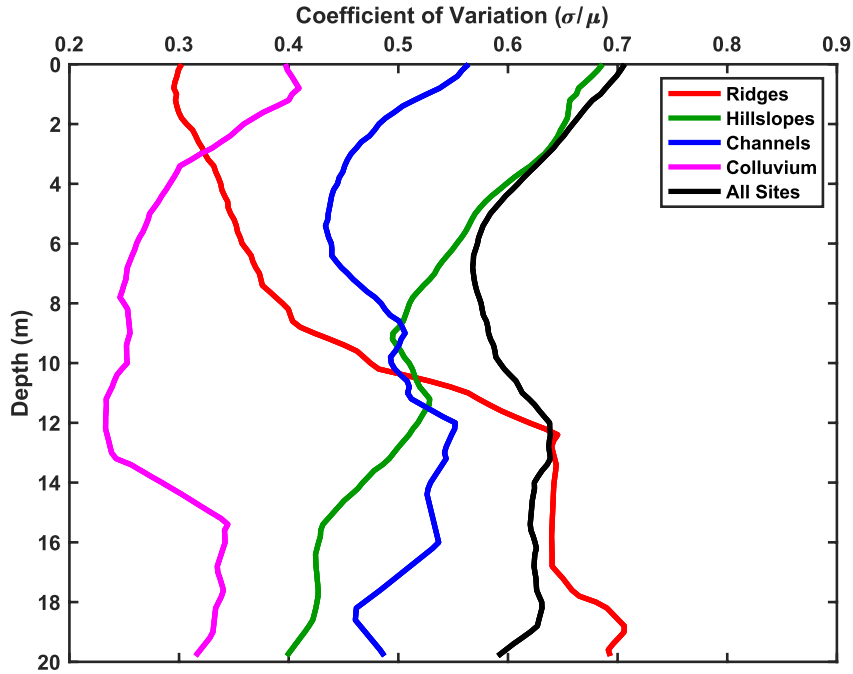

Figure 7. Coefficient of variation (COV) in V_s among bedrock sites on ridges, hillslopes, near bedrock channels, as well as surveys on unconsolidated colluvium. The high COV values near the surface are partially attributed to the higher resolution of the multichannel analysis of surface wave (MASW) technique near the surface (Greenwood et al., 2015), but also reflect a greater variability in the degree of weathering at the surface compared to depth, especially among hillslope sites.

the median profile ranging from 350 to 1,500 m/s at 20 m, and channel site shear strength predictions are 1–2 orders of magnitude higher compared to ridge sites (median profile 1 MPa at the surface to 3 MPa at 20 m depth). The importance of chemical alteration is highlighted in the difference between the ridge and channel GSI charts (Figure 6, left column), which is driven more by the surface quality descriptor (horizontal axis) rather than the structure of the discontinuities (vertical axis).

In all cases, the categorization of topographic position (i.e., ridge, hillslopes, channels) for rock sites and the separation of colluvium from rock sites reduces the COV in V_s for at least some portion of the profile, thereby identifying key characteristics that may explain site-to-site differences in data values (Figure 7). Colluvium V_s profiles are least variable and are characterized by a COV well below 0.4 for much of the profile, which reflects the more uniform properties of unconsolidated material compared to weathered bedrock. Among the rock sites, the COV is more uniformly distributed with respect to depth for channel sites than it is for those on ridges or hillslopes, potentially reflecting a more uniform weathering gradient with depth among channel sites. V_s profiles on hillslopes show the highest normalized variance at the surface, which likely reflects the wide range of weathering conditions characterizing bedrock at these sites. The bedrock ridge V_s profiles are unique in that they are most variable at depths below ~10 m, with significantly lower COV values in the shallow (<10 m) part of the profile. We suggest this jump in variance among ridge V_s profiles below ~10 m is reflective of variation in the depth to unweathered rock on ridge sites at different locations. While all ridge sites are characterized by low velocities (<500 m/s) and highly weathered rock at the surface (very poor to fair surface quality ratings, Figure 6), several of the ridge V_s profiles ($n = 5$) transition to largely unweathered rock velocities (>750 m/s) at depths below ~10 m, thereby driving a jump in variance among ridge surveys in the aggregate.

4.2. Variations in Bedrock Characteristics With Respect to Metamorphic Grade

Lithologic variation is primarily related to differences in metamorphic grade among the metasedimentary rocks surveyed. Most of our sites were collected in schist or gneiss, with less than 10 surveys collected in either phyllite or slate, and 17 V_s surveys on unconsolidated colluvium (Figure 8). The mechanical properties for slates, phyllites, schists, and gneiss do not show systematic trends with respect to increasing grade, although it is important

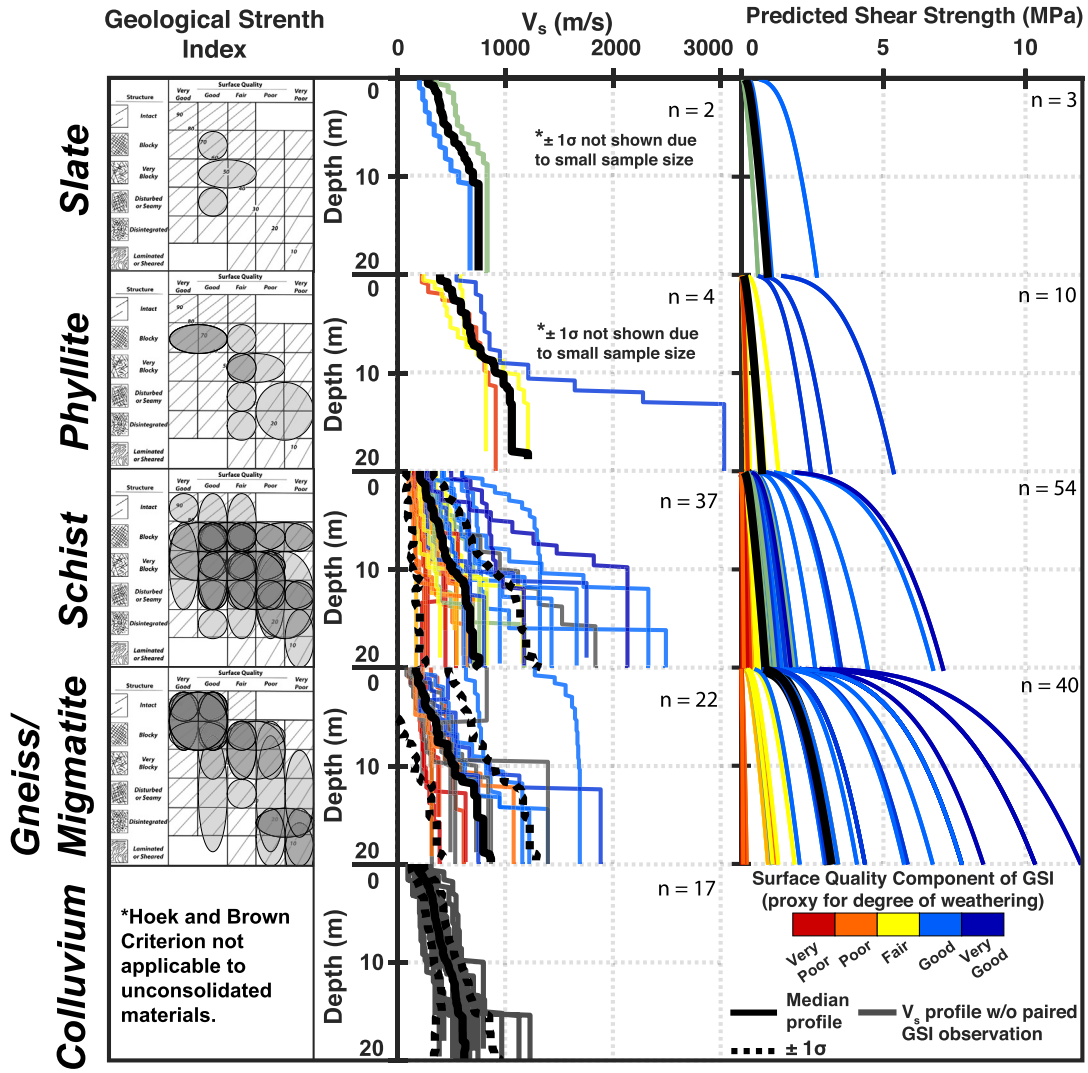

Figure 8. Classification of field surveys by metamorphic grade where the color of the V_s and shear strength profiles indicates the surface quality component of the geological strength index observation at that site. In general, the degree of weathering causes larger differences in V_s compared to the differences in lithology documented here.

to note that this result is qualified by the small number of observations for slates and phyllites compared to the higher grade lithologies. Slates and phyllites tend to have moderate strength and V_s compared to schists and gneisses and, notably, also have similarly low COV values for both V_s30 and GSI compared to the data set overall (Table 1). The median V_s profiles are similar in the upper few meters (~350–450 m/s) and increase to 750 m/s and 1,050 m/s at 20 m depth for slates and phyllites respectively. Mean and standard deviation for GSI is 53 ± 9 for slates and 47.5 ± 19 for phyllites, resulting in shear strength predictions with a median of 0.93 and 0.73 MPa at 20 m depth for the two rock types respectively. Gneisses and migmatites have lower median V_s values at shallow depths than phyllites (~200 m/s) but increase to similar values at depth (~850 m/s at 20 m depth) with also slightly higher mean GSI values (56 ± 26). The median shear strength is predicted to be 3.1 MPa at 20 m depth, giving gneisses the highest predicted shear strength out of all the lithologies surveyed. In contrast, we observe the lowest average velocity profile, GSI values, and shear strength predictions among schists. The average V_s profile ranges from ~200 m/s at the surface to ~700 m/s at 20 m depth, average and standard deviation for GSI is 46 ± 17, and the median shear strength is 0.85 MPa at 20 m depth. Colluvium sites produce more consistent velocity profiles than the bedrock sites, with a slower median value extending from ~200 m/s at the surface to ~600 m/s at 20 m depth.

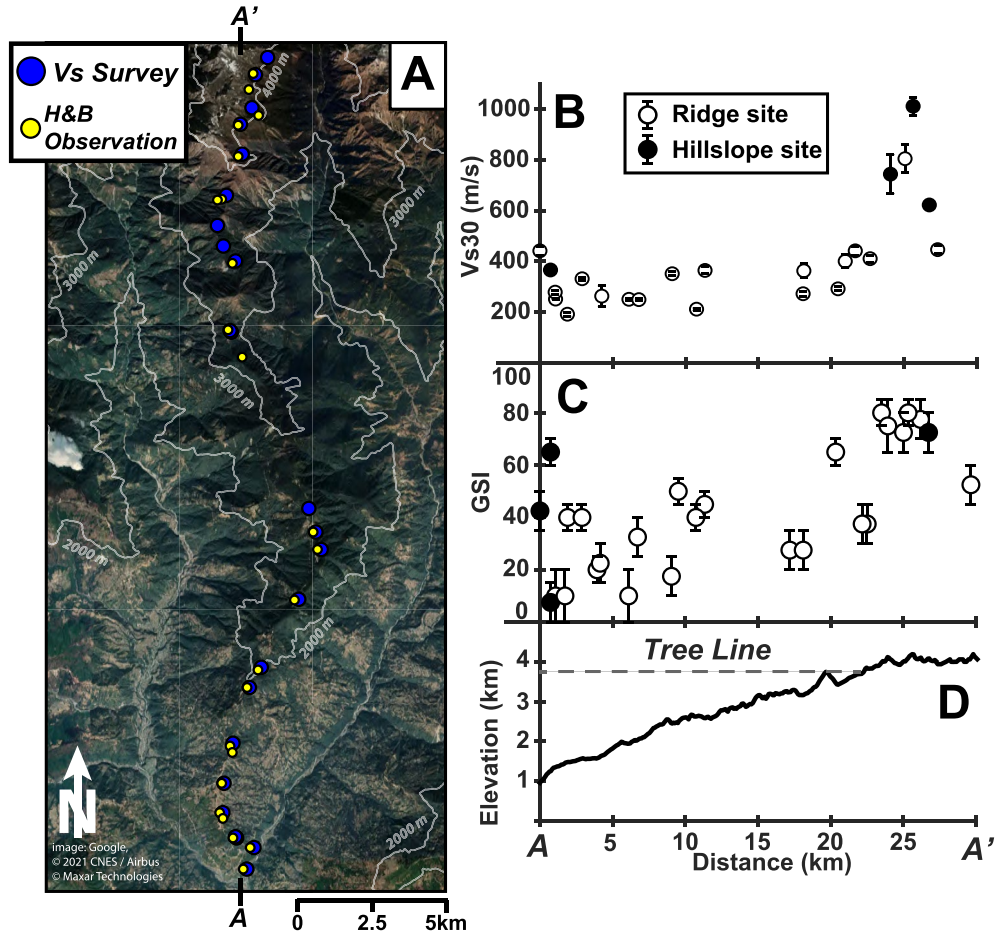

Figure 9. (a) Field survey transect along the eastern Melamchi Khola drainage divide spanning 1.2–4.2 km elevation. Satellite image from Google Earth. (b) V_s30 projected along north-south line indicated by A-A'. Error bars correspond to the standard deviation in V_s30 based on the 300 lowest-misfit inversion profiles. (c) Geological strength index (GSI) values projected along same line of section, with error bars corresponding to the field-estimated range in GSI for each outcrop (d) Topographic profile along sampling transect based on SRTM 30 m DEM. Tree line altitude is approximately 3,900 m (Schickhoff, 2005), above which there is an abrupt increase in V_s30 values reflecting the limited weathering conditions at alpine elevations.

4.3. Melamchi Khola Elevation Transect

To evaluate rock strength along a cross-range profile extending into the Greater Himalayan physiographic region we surveyed a dense transect of sites ranging from 1.2 to 4.2 km elevation along the western drainage divide of the Melamchi River catchment (Figures 1 and 9). All sites along this transect are characterized by Himal Group gneisses and schists, and all but four sites were located on ridges. For the V_s data, we find remarkably consistent and low V_s30 values of ~300 m/s over ~20 km distance, reflecting the consistently highly weathered nature of the bedrock along the ridge. However, for elevations above the alpine tree line (~3.9 km in central Nepal; Schickhoff, 2005), we encountered visibly less chemically altered material, thinner soil mantle, and a significant increase in V_s30 values, to as high as 1,100 m/s, which is well within the engineering site classification for hard rock (site class A, FEMA, 2004). Unfortunately, the transition to terrain above tree line also coincided with much more challenging access to the main Melamchi drainage divide (the trail turned away from the ridge). As a result, the limited weathering conditions we found at high elevations may reflect the fact that these sites were close to the ridge line, but technically on hillslopes. However, two of the six Melamchi sites above 4,000 m were on minor ridges and still produced velocities characteristic of hard rock, which is consistent with the interpretation that alpine elevations and the associated change in climate and vegetation are the main factors responsible for the limited weathering conditions.

We also find an increase in GSI with increasing elevation, although these data show a comparatively larger variance than the V_s data and without the clear stepwise jump in values above tree line elevations (Figure 9). We suggest the greater variability in the GSI observations compared to the V_s data results from the smaller sampling scale cast by the GSI outcrop descriptions, which can be biased by meter scale variability in rockmass characteristics that may not be representative of the kilometer scale patterns in weathering along the transect. Considering the consistency of the outcrops we described above tree line (GSI values over 70 for 6 of 7 the outcrops we characterized) we argue that our GSI data are consistent with a threshold change in weathering conditions above tree line altitudes.

4.4. Climate Control on Bedrock Mechanical Properties

Where erosion rates are fast enough to keep pace with chemical weathering and maintain a supply of unweathered material—as is the case in the Himalaya—rates of chemical weathering depend on reaction kinetics that are influenced by several parameters including ambient temperature and water flow rates (Bluth & Kump, 1994; Kump et al., 2000; West et al., 2005). Mean annual temperature (MAT) and mean annual precipitation (MAP) are therefore commonly cited as predictors of chemical weathering rates and critical zone thickness (Anderson et al., 2013; Lebedeva & Brantley, 2013; Rempe & Dietrich, 2014; Von Voigtlander et al., 2018). We compare our field surveys to annualized precipitation data recorded by the TRMM satellite mission (Bookhagen & Burbank, 2010), and annualized temperature estimated based on an average atmospheric lapse rate for the central Himalaya (Kattel et al., 2013; Figure 10). We further subdivide the data by plotting sites on ridges, hillslopes, and channels separately in order to control for the systematic variations in weathering related to topographic location. First-order correlations between MAP and chemical weathering rates in global datasets (e.g., White & Blum, 1995) led us to predict a negative correlation between our mechanical competence metrics and MAP. Yet instead, we observe a weak trend of increasing rock strength with increasing MAP for ridge and channel sites (i.e., suggesting less chemical weathering where MAP is higher). This trend is opposite of that expected if chemical weathering were limited only by the availability of water. However, Figure 10 also shows that MAT tends to decrease with increasing MAP, owing to opposite dependencies on the orographic effect (MAT decreases while MAP increases with elevation in our study region). Indeed, the weak positive correlations between MAP and the ridge GSI and V_s data ($R^2 = 0.1$ and 0.3, respectively) are mostly driven by a small number of sites in alpine terrain where the MAT is near freezing, and thus chemical weathering conditions are likely constrained by the lack of vegetation and cold temperatures rather than the availability of water.

Interestingly, we also find a positive correlation between MAP and V_s30 for channel sites despite the fact that all of these sites are located at low elevations with uniformly warm MAT (Figure 10f). While this correlation is qualified by the small number of observations ($n = 10$), we postulate that the observed increase in V_s near channels with increasing MAP may be a consequence of a general spatial coincidence between MAP and erosion rates, which are highest along the southern flanks of the Himalaya north of the physiographic transition (PT_2). We speculate that the high erosion rates north of PT_2, which may itself be influenced by high MAP, drive high V_s in the near surface by stripping away weathered material near the channel before it accumulates.

5. Discussion

A central goal of this study is to understand the magnitude of regional variability in near-surface strength properties in tectonically active landscapes, as well as the primary sources of that variability. To this end, we found an order-of-magnitude variability in rockmass strength that is mostly driven by the degree of chemical and physical weathering. Regardless of rock type, our results show that unweathered or lightly weathered bedrock outcrops generally correspond to shear wave velocities that surpass 1,000 m/s, while bedrock with clear signs of chemical alteration extend into velocities below 300 m/s—values that are typically thought of as more characteristic of soil rather than rock (Figure 8). While the observation that rock strength is degraded by chemical and physical weathering is not a new result by itself, our results demonstrate how variable the degree of weathering can be over landscape scales, and we are able to show that this variability is related to factors such as topographic position. Our work highlights the importance of evaluating weathering characteristics across a landscape for accurate estimation of rock strength in landslide hazard or bedrock erodibility applications.

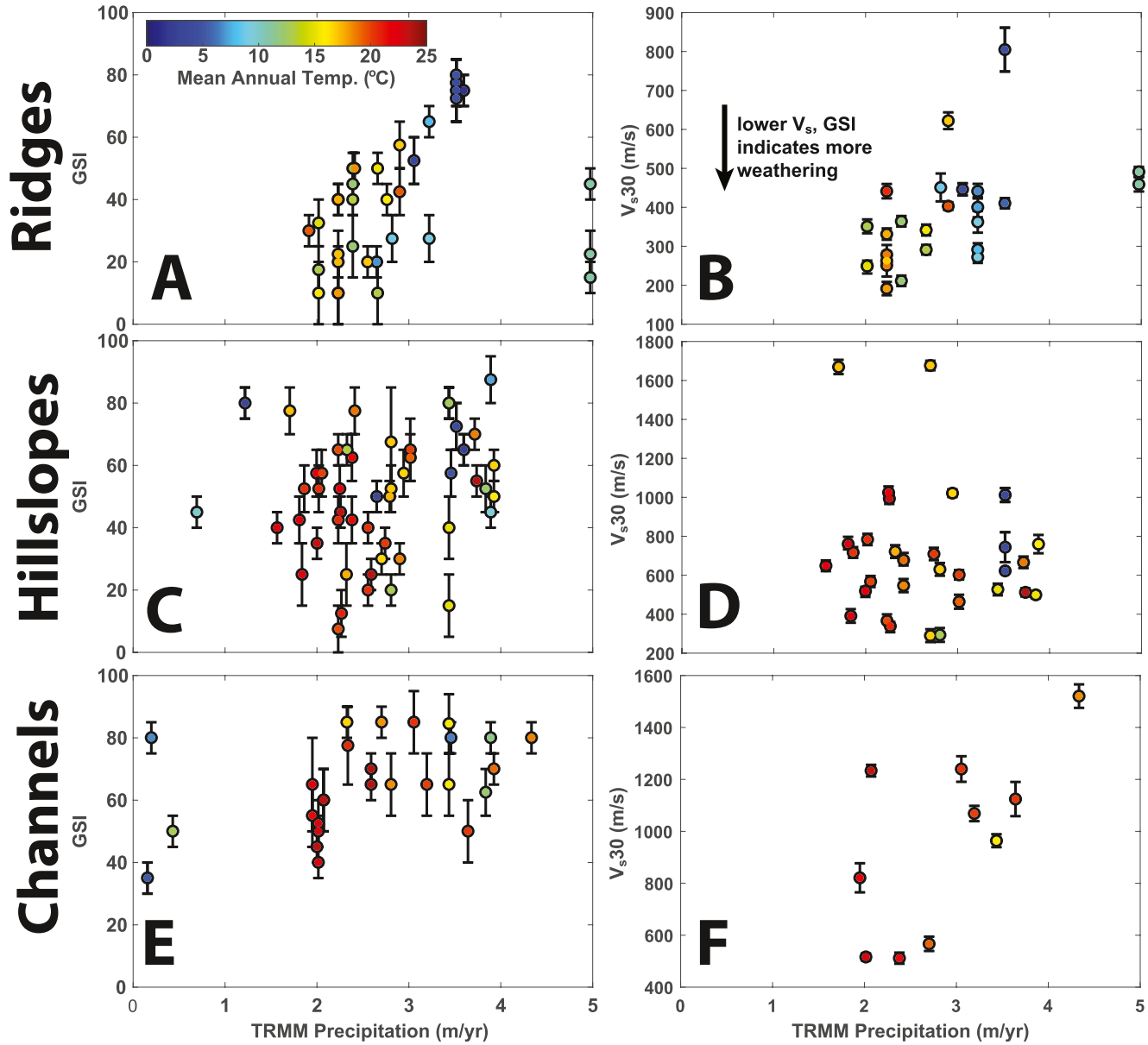

Figure 10. Comparison between mean annual precipitation (MAP) and geological strength index (GSI) and V_s30 as a function of mean annual temperature (MAT) and topographic position. MAP estimates reflect the average over the period 1998–2009 measured by the TRMM satellite mission (Bookhagen & Burbank, 2010). MAT was estimated based on the elevation of each site using the best-fit lapse rate for the Himalaya (Kattel et al., 2013). Error bars in b, d, and f correspond to the standard deviation in V_s30 based on the 300 lowest-misfit inversion profiles, and error bars for a, c, and e correspond to the field-estimated range in GSI for each outcrop.

5.1. Variations in Weathering With Respect to Ridges, Channels, and Hillslopes

Of the variables we assessed, the strongest predictor of chemical and physical weathering, and by extension rock strength, is the location of the rockmass with respect to ridge-channel topography. This result is consistent with previous studies that have observed the deepest subsurface extent of chemically altered and fractured rock under ridges and thinnest extent under valley bottoms (Pedrazas et al., 2021; St. Clair et al., 2015). The two leading mechanisms invoked to explain this pattern are a topographic stress control on bedrock fractures (Moon et al., 2017; Slim et al., 2015; St. Clair et al., 2015), and the subsurface topography of the water table (Rempe & Dietrich, 2014). Although these mechanisms are not mutually exclusive, we suggest that topographic stress-induced fractures are likely to be particularly relevant in the Himalaya, not only due to the dramatic scale of the topography but also because of the strong regional compressive stress which has been previously shown

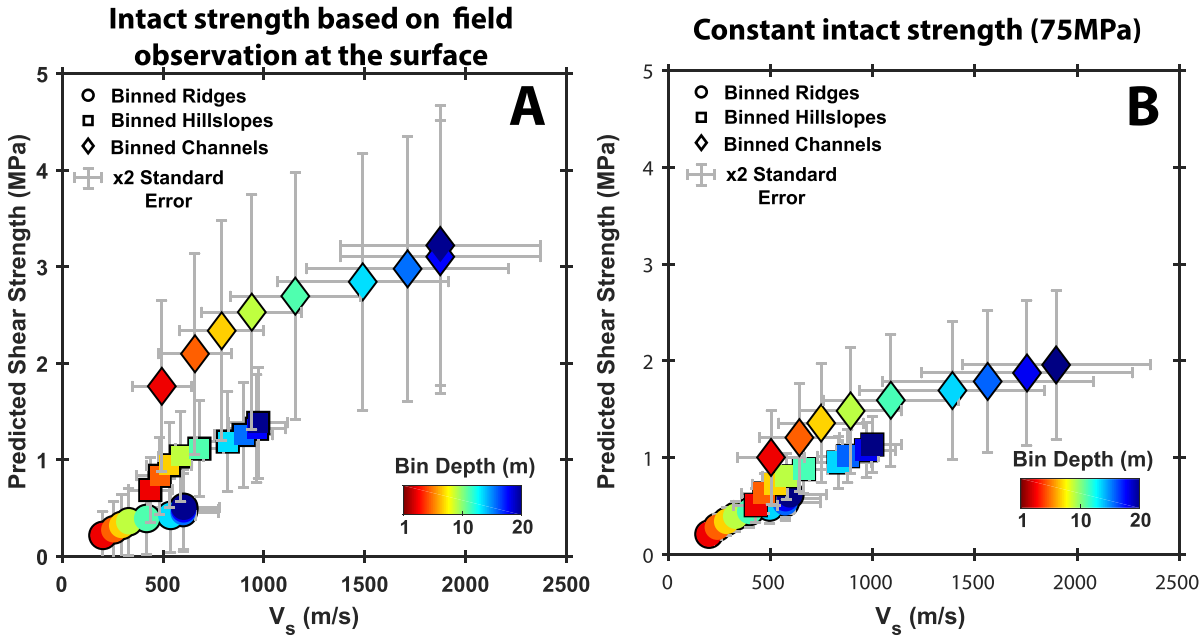

Figure 11. Mean shear strength against mean S-wave velocity profiles of all bedrock data, calculated by binning the profiles in 2 m intervals. Error bars are twice the standard error on the mean value in each bin. Notably, in both cases there appears to be a decrease in strength-V_s gradient at about V_s = 1,000 m/s, which reflects the non-linear shape of the Hoek–Brown failure criterion.

to determine the extent to which ridges are more-weathered than channels (Moon et al., 2017; Slim et al., 2015; St. Clair et al., 2015). Another factor that might contribute to topographic-dependent bedrock fractures is topographic-amplification of seismic rock damage induced during the recent 2015 Gorkha Earthquake (e.g., Huang et al., 2019), although we note that previously documented reductions in shallow seismic velocity following large earthquakes are generally less than 5%, which is far less than the factor of ~2 difference we observe in the median V_s profiles for ridge versus channel sites (Hobiger et al., 2016; Marc et al., 2021; Takagi et al., 2012). The specific mechanism notwithstanding, the strength of the correlation between the degree of weathering and proximity to ridges, channels, and hillslopes is an important result because it suggests that the geomorphic control on chemical and physical bedrock weathering dominates over other environmental variables. We are unaware of any previous studies that have demonstrated the relative strength of this control compared to other environmental variables at regional scales, particularly in landscapes characterized by the topographic relief of the Himalaya.

We also gain insight into the effect of topography on weathering by examining the relationship between predicted shear strength and S-wave velocity. For each topographic category (ridges, hillslopes and channels), we observe a positive relationship between shear strength and V_s, with increasing ranges of values from ridges to channels (Figure 11). Both V_s and shear strength increase as a function of depth, in part due to the increase in confining stress due to the overburden, as well as the likely fact that fracture density/quality and chemical weathering typically decrease with increasing depth. In reality, confining stress and the depth-weathering profile should both contribute to the observed positive relationship; however, it is important to point out here that the methodology of predicting the shear strength-depth profile described in Section 3.2.2 makes a deliberate choice about the intact strength based on the outcrop observation. Using surface information to project strength at depth lacks consideration that weathering typically decreases with depth, and instead the predicted depth changes are solely based on increases in confining stress. Using a constant value for intact strength (σ_{ci}) compared to measured field values produces a lower strength- V_s gradient and more consistent values between ridges, hillslopes and channels. For example, using an "average" intact strength value of 75 MPa, channels and hillslopes have lower strengths for a given V_s, while ridges have slightly higher values compared to using intact strength measured at outcrops. However, we note that the relative direction that the values change (increasing or decreasing strength) is dependent on the choice of constant strength. Although we cannot know the weathering profile a priori, we can bound the shear-strength to V_s relationship by comparing the shear-strength/V_s relationship calculated with measured intact values from outcrops to using a constant value (Figure 11). The consistency of this relationship implies a continuum of

physical properties that relate to topographic position, where mechanical competence decreases and weathering increases. The uncertainty envelope of this relationship can be used to estimate the shear strength within less than a factor of two. Such estimates are of value to future hazard studies as well as landscape evolution modeling.

5.2. Threshold Variation in Near-Surface Characteristics With Respect to Elevation and Slope Gradient

In addition to the strong topographic signal in our data, we also find that elevation and slope gradient help to explain some of the variability we observe in weathering. We find relatively low COV values in both the V_s30 and GSI data for sites above tree line (~3.9 km in central Nepal; Schickhoff, 2005), and those on slopes steeper than 35° (Table 1). On the other hand, we find sites on slopes gentler than 35°, or those below tree line elevations, show no reduction in COV when they are separated out from the rest of the data set. This result suggests that slope gradient and elevation cause threshold changes to near-surface weathering and fracturing rather than a gradual control. This interpretation is further supported by our V_s transect along the Melamchi drainage divide (Figures 1 and 9), where we found nearly constant V_s30 values along ~20 km of the transect with an abrupt increase in V_s at elevations above 3.9 km.

A transition in weathering rates above tree line is likely caused by several factors. First, the cold temperatures at alpine elevations slow weathering kinetics (Kump et al., 2000). Using the Arrhenius equation, Riebe et al., (2004) found that a 4°C decrease in MATs theoretically causes a 32% decrease in the chemical depletion factor for outcrops at the surface. Furthermore, the scarcity of vegetation at high altitudes is known to retard the rate of chemical and physical weathering by reducing the potential for root throw, limiting the availability of organic acids, and restricting the hydraulic storage capacity in the subsurface (Riebe et al., 2004). An additional, although less certain factor, is the relatively recent retreat of glaciers and perennial snowpack from modern periglacial altitudes in the Himalaya since the last glacial maximum (LGM) ended at ~20 ka (Owen & Benn, 2005). Modeling indicates that the timescale for transient evolution of the weathering profile to changing conditions can be of the same order as the time since the LGM (Anderson et al., 2019) meaning that it is possible that some of our high elevation sites may be characteristic of weathering conditions during previous glacial cycles, or at least in transient adjustment out of those conditions.

High erosion rates may also contribute to the limited weathering conditions characterizing our high elevation sites. Numerous studies have now demonstrated that a kinetic limitation on the weathering rate develops when the physical erosion rate increases to a point where fresh minerals are eroded away faster than the timescale for weathering reactions (Dixon et al., 2012; Ferrier & Kirchner, 2008; West et al., 2005). Thus, rapidly eroding parts of the landscape may be characterized by bare rock at the surface with little chemical alteration, as weathering reactions are too slow to keep pace with the denudation. We suggest that this may be the case for our alpine sample sites, which also happen to be farthest northeast of the MCT where previous studies have documented the highest uplift and erosion rates in the Himalaya (Bilham et al., 1997; Grandin et al., 2012; Herman et al., 2010). In these northern areas above treeline, rapid erosion rates may be facilitated by a largely mechanical weathering system driven by freeze-thaw cycles rather than chemical degradation of the rockmass.

5.3. Relation Between Rock Mechanical Properties and Metamorphic Grade

Although we largely controlled for lithology by focusing all our bedrock surveys on crystalline metamorphic rocks of sedimentary origin, our survey sites do span a range of metamorphic grades, and it stands to reason that the associated differences in index minerals, grain size, and fabric characteristics influence the inherent mechanical properties of the rockmass and susceptibility to weathering. However, when organized by increasing metamorphic grade we did not observe systematic changes in the median V_s or predicted strength profiles within the statistical limits (Figure 8). Furthermore, we found a large internal variability in mechanical characteristics within the same metamorphic grade. Both schist and gneiss outcrops display nearly the full extent of possible GSI values (<10 to >90), and V_s profiles in both rock types range by over 1,000 m/s in at depths below 10 m (Figure 8). We interpret this variability to reflect primarily the large range in weathering conditions observed across outcrops, which dominate the mechanical properties compared to differences in grain size, texture, and mineral assemblages related to metamorphic grade.

To be clear, we do not mean to suggest that rock strength is completely independent of metamorphic characteristics. There may well be systematic variations in rock strength and susceptibility to weathering present in our

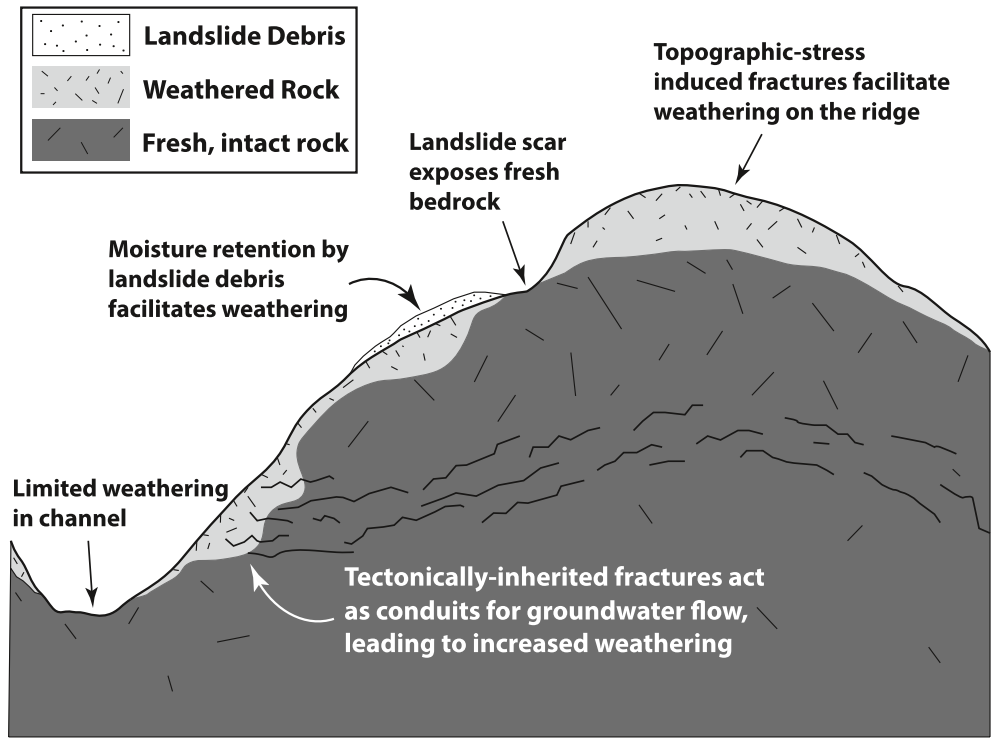

Figure 12. Conceptual model of subsurface properties in a steep, mountain landscape. Previous studies have established the pattern of ridges being more deeply weathered than bedrock channel bottoms (Rempe & Dietrich, 2014; St. Clair et al., 2015), and that tectonically or topographically induced deep fractures facilitate concentrated chemical weathering along the fracture network (Holbrook et al., 2019). We speculate here that bedrock landslides may provide another mechanism for variability in chemical weathering by periodically clearing away weak and weathered material on hillslopes. The weathering profile is thus "reset" under recent landslide scars.

observations, but we lack the statistical power to resolve these differences clearly. For example, the abundance of low V_s and shear strength profiles for schists compared to the other metamorphic categories (Figure 8) is consistent with our qualitative field observation that schist outcrops are commonly characterized by a large proportion of weak and friable muscovite, so it may be a reflection of a true systematic difference despite the statistical uncertainty. Similarly, we qualitatively observed slate and phyllite outcrops to be generally more homogeneous in terms of mineral content and grain size compared to schists and gneisses, so it may be sensible that they correspond to lower COV values for V_s30 and GSI. However, with only 10 or fewer measurements in slates and phyllites we are cautious to over-interpret this result. We also emphasize that our results may not apply to other landscapes, and particularly those characterized by greater lithologic diversity than our study area. Indeed, previous studies indicate that rock strength parameters and weathering susceptibility can vary strongly as a function of lithology, particularly in arid landscapes characterized by sedimentary rock sequences (Bursztyn et al., 2015; Duvall et al., 2004; Townsend et al., 2021). However, such ranges in lithology (e.g., shale vs. sandstone) potentially represent significantly greater differences in mineral content, porosity, and grain characteristics compared to the high-grade metamorphic schists and gneisses that characterize the majority of our observations.

5.4. Why Are Rock Properties More Variable on Hillslopes Than Near Ridges or Channels?

Compared to our observations on ridges and channels, the hillslope site observations are characterized by much greater variability in rockmass mechanical characteristics and the degree of chemical weathering (Figure 6). While it is likely that this variability partially reflects the other regional-scale factors that we have not controlled for, we also observed the same pattern after restricting our analysis to a single lithology (Section S2 in Supporting Information S1). Explaining the high variability in hillslope weathering may therefore involve local factors operating over the scale of individual hillslopes. Figure 12 summarizes several such mechanisms proposed by previous studies. For example, Gabet (2007) proposed that the maturity of the weathering profile should be highly

variable in the hillslope environment depending on the time since the last bedrock landslide. Given the very high landslide rates in central Nepal (Marc et al., 2019), we speculate that our high-V_s and high-GSI hillslope sites may represent locations where the weathered bedrock and regolith has been stripped away by geologically recent landslides to expose fresher and mechanically stronger bedrock at the surface (Figure 12). Additionally, we posit that the hillslope-scale variability in deep fracture networks and foliation may also contribute to the site-to-site variability we found in bedrock strength (Figure 12). Fractures and foliations induced by tectonic stresses can penetrate much more deeply into the subsurface than fractures caused by top-down processes such as frost cracking, thermal cycles, or root throw (Clarke & Burbank, 2010), and they provide conductive pathways for reactive meteoric fluids to infiltrate the bedrock and create heterogeneous concentrations of weathered material (Holbrook et al., 2019; Leone et al., 2020). We propose that another contributing factor could be variations in the thickness of soil and unconsolidated colluvium mantling the hillslope environment. The hydraulic storage capacity of low permeability soils and colluvial mantle should influence mineral alteration in the saprolite horizon at depth by changing water residence time in the shallow subsurface (Dixon et al., 2012; Green et al., 2006). This mechanism may lead to especially complex patterns in chemical weathering on hillslopes when the colluvial cover is redistributed through the action of landsliding (Figure 12). While we lack the directed field observations to assess the specific impact of these mechanisms on our results, we suggest that future estimates of regional-scale rock strength should acknowledge the likelihood of hillslope-scale variability and make the appropriate allowances in uncertainty.

6. Conclusions

We have quantified regional-scale trends and variability in bedrock mechanical properties across central Nepal using shallow seismic surveys and Hoek and Brown's GSI classification system. While no single mechanism is sufficient to explain the detailed characteristics of the weathering profile at specific sites, we find that correlations with ridge to channel topography and weathering patterns are robust across the study area. Consistent with previous studies, we find that bedrock on ridges tends to be highly weathered and has V_s and shear strength characteristics more typical of stiff soils, whereas sites near the bedrock channel bottom tend to be unweathered and characterized by high shear wave velocities and shear strength estimates typical of hard rock. An exception to this pattern is observed at elevations above tree line elevations, where we find a limited degree of chemical weathering among ridge sites, likely reflecting the slow weathering kinetics in the colder climate and the limited availability of organic acids in the thin soils of the alpine ecosystem. Finally, we find that lithology plays a secondary role in determining rock strength, although the relative similarity of the rocks surveyed (all crystalline metasedimentary lithologies) may make this result unique to the central Himalaya.

Our results demonstrate that chemical weathering can create order-of-magnitude variability in the shallow subsurface strength profile in tectonically active landscapes. This variability and its spatial structure directly affect patterns in landsliding, fluvial network dynamics, and thus ultimately patterns in weathering itself. In terms of implications for applied studies, we suggest that even a cursory representation of systematic patterns in chemical and physical weathering would significantly improve rock strength estimates for regional landslide hazard assessment and landscape evolution models. Lastly, we suggest that our use of portable and relatively inexpensive geotechnical techniques provides a framework for future empirical investigations of bedrock weathering and near-surface strength over landscape scales.

Conflict of Interest

The authors declare no conflicts of interest relevant to this study.

Data Availability Statement

All raw seismic data, dispersion curve interpretations, V_s profiles, GSI observations, field notes, and a ReadMe file are available from the University of Michigan DeepBlue data repository (accessible at https://doi.org/10.7302/s6sw-k853) with license CC BY-NC 4.0.

Acknowledgments
We are grateful for detailed and thoughtful reviews of an earlier version of the manuscript by Netra Prakash Bhandary and two other anonymous reviewers, and the associate editor Matt Brain. We also thank the editor Mikael Attal. W. G. Medwedeff received support from a National Science Foundation (NSF) Graduate Research Fellowship (Fellow ID 2018261637). The work was also supported by NSF grants to M. K. Clark, D. Zekkos, and A. J. West (NSF-EAR 1640797 and 1640894). We thank Raju Kunwar, Suman Budhathoki, Sabin Tiwari, Logan Knoper, Paul Quackenbush, Abra Atwood, and Max and Dhalquist for assistance in the field. We also thank Sylvain Pasquet for his generous technical support using SWIP.

References

Anderson, R. S., Anderson, S. P., & Tucker, G. E. (2013). Rock damage and regolith transport by frost: An example of the climate modulation of the geomorphology of the critical zone. *Earth Surface Processes and Landforms*, *38*(3), 299–316. https://doi.org/10.1002/esp.3330

Anderson, R. S., Rajaram, H., & Anderson, S. P. (2019). Climate driven coevolution of weathering profiles and hillslope topography generates dramatic differences in critical zone architecture. *Hydrological Processes*, *33*, 4–19. https://doi.org/10.1002/hyp.13307

Anderson, S. P., Anderson, R. S., & Tucker, G. E. (2012). Landscape scale linkages in critical zone evolution. *Comptes Rendus Geoscience*, *344*(11–12), 586–596. https://doi.org/10.1016/j.crte.2012.10.008

Anderson, S. P., Hinckley, E. L., Kelly, P., & Langston, A. (2014). Variation in critical zone processes and architecture across slope aspects. *Procedia Earth and Planetary Science*, *10*, 28–33. https://doi.org/10.1016/j.proeps.2014.08.006

Anderson, S. P., von Blanckenburg, F., & White, A. F. (2007). Physical and chemical controls on the critical zone. *Elements*, *3*(5), 315–319. https://doi.org/10.2113/gselements.3.5.315

Befus, K. M., Sheehan, A. F., Leopold, M., Anderson, S. P., & Anderson, R. S. (2011). Seismic constraints on critical zone architecture, Boulder Creek Watershed, Front Range, Colorado. *Vadose Zone Journal*, *10*, 915–927. https://doi.org/10.2136/vzj2010.0108

Bilham, R., Larson, K., & Freymueller, J. (1997). GPS measurements of present-day convergence across the Nepal Himalaya. *Nature*, *386*, 61–64. https://doi.org/10.1038/386061a0

Bluth, G. J., & Kump, L. R. (1994). Lithologic and climatologic controls of river chemistry. *Geochimica et Cosmochimica Acta*, *58*(10), 2341–2359. https://doi.org/10.1016/0016-7037(94)90015-9

Bookhagen, B., & Burbank, D. W. (2010). Toward a complete Himalayan hydrological budget: Spatiotemporal distribution of snowmelt and rainfall and their impact on river discharge. *Journal of Geophysical Research*, *115*, F03019. https://doi.org/10.1029/2009JF001426

Bursztyn, N., Pederson, J. L., Tressler, C., Mackley, R. D., & Mitchell, K. J. (2015). Rock strength along a fluvial transect of the Colorado Plateau – Quantifying a fundamental control on geomorphology. *Earth and Planetary Science Letters*, *429*, 90–100. https://doi.org/10.1016/j.epsl.2015.07.042

Clarke, B. A., & Burbank, D. W. (2010). Bedrock fracturing, threshold hillslopes, and limits to the magnitude of bedrock landslides. *Earth and Planetary Science Letters*, *297*(3–4), 577–586. https://doi.org/10.1016/j.epsl.2010.07.011

Clarke, B. A., & Burbank, D. W. (2011). Quantifying bedrock-fracture patterns within the shallow subsurface: Implications for rock mass strength, bedrock landslides, and erodibility. *Journal of Geophysical Research: Earth Surface*, *116*(4). https://doi.org/10.1029/2011JF001987

DeCelles, P. G., Robinson, D. M., Quade, J., Ojha, T. P., Garzione, C. N., Copeland, P., & Upreti, B. N. (2001). Stratigraphy, structure, and tectonic evolution of the Himalayan fold-thrust belt in western Nepal. *Tectonics*, *20*(4), 487–509. https://doi.org/10.1029/2000tc001226

Dixon, J. L., Hartshorn, A. S., Heimsath, A. M., DiBiase, R. A., & Whipple, K. W. (2012). Chemical weathering response to tectonic forcing: A soils perspective from the San Gabriel Mountains, California. *Earth and Planetary Science Letters*, *323–324*, 40–49. https://doi.org/10.1016/j.epsl.2012.01.010

Duvall, A., Kirby, E., & Burbank, D. (2004). Tectonic and lithologic controls on bedrock channel profiles and processes in coastal California. *Journal of Geophysical Research*, *109*, F03002. https://doi.org/10.1029/2003JF000086

Eppes, M. C., Hancock, G. S., Chen, X., Arey, J., Dewers, T., Huettenmoser, J., et al. (2018). Rates of subcritical cracking and long-term rock erosion. *Geology*, *46*(11), 951–954. https://doi.org/10.1130/g45256.1

Federal Emergency Management Agency (FEMA) (2004). *NEHRP recommended provisions for seismic regulations for new buildings and other structures, Part 1: Provisions (FEMA 450-2), 2003 edition*. Building Seismic Safety Council, National Institute of Building Sciences.

Ferrier, K. L., & Kirchner, J. W. (2008). Effects of physical erosion on chemical denudation rates: A numerical modeling study of soil-mantled hillslopes. *Earth and Planetary Science Letters*, *272*, 591–599. https://doi.org/10.1016/j.epsl.2008.05.024

Forte, A. M., Yanites, B. J., & Whipple, K. X. (2016). Complexities of landscape evolution during incision through layered stratigraphy with contrasts in rock strength. *Earth Surface Processes and Landforms*, *41*(12), 1736–1757. https://doi.org/10.1002/esp.3947

Foti, S., Comina, C., Boiero, D., & Socco, L. V. (2009). Non-uniqueness in surface-wave inversion and consequences of seismic site response analyses. *Soil Dynamics and Earthquake Engineering*, *29*(6), 982–993. https://doi.org/10.1016/j.soildyn.2008.11.004

Frattini, P., & Crosta, G. B. (2013). The role of material properties and landscape morphology on landslide size distributions. *Earth and Planetary Science Letters*, *361*, 310–319. https://doi.org/10.1016/j.epsl.2012.10.029

Gabet, E. J. (2007). A theoretical model coupling chemical weathering and physical erosion in landslide dominated landscapes. *Earth and Planetary Science Letters*, *264*(1–2), 259–265. https://doi.org/10.1016/j.epsl.2007.09.028

Gallen, S. F. (2018). Lithologic controls on landscape dynamics and aquatic species evolution in post-orogenic mountains. *Earth and Planetary Science Letters*, *493*, 150–160. https://doi.org/10.1016/j.epsl.2018.04.029

Gansser, A. (1964). *Geology of the Himalayas* (p. 289). Interscience.

Garofalo, F., Foti, S., Hollender, F., Bard, P. Y., Cornou, C., Cox, B. R., et al. (2016). InterPACIFIC project: Comparison of invasive and non-invasive methods for seismic site characterization, Part I: Intra-comparison of surface wave methods. *Soil Dynamics and Earthquake Engineering*, *82*, 222–240. https://doi.org/10.1016/j.soildyn.2015.12.010

Gilbert, G. K. (1877). *Geology of the Henry Mountains* (p. 160). US Geographical and Geological Survey.

Grandin, R., Doin, M. P., Bollinger, L., Pinel-Puyssegur, B., Ducret, G., Jolivet, R., & Sapkota, S. N. (2012). Long-term growth of the Himalaya inferred from interseismic InSAR measurement. *Geology*, *40*(12), 1059–1062. https://doi.org/10.1130/g33154.1

Green, E. G., Dietrich, W. E., & Banfield, J. F. (2006). Quantification of chemical weathering rates across an actively eroding hillslope. *Earth and Planetary Science Letters*, *242*(1–2), 155–169. https://doi.org/10.1016/j.epsl.2005.11.039

Greenwood, W., Zekkos, D., & Sahadewa, A. (2015). Spatial variation of shear wave velocity of waste materials from surface wave measurements. *Journal of Environmental & Engineering Geophysics*, *20*(4), 287–301. https://doi.org/10.2113/jeeg20.4.287

Gu, X., Rempe, D. M., Dietrich, W. E., West, A. J., Lin, T., Jin, L., & Brantley, S. L. (2020). Chemical reactions, porosity, and microfracturing in shale during weathering: The effect of erosion rate. *Geochimica et Cosmochimoca Acta*, *269*, 63–100. https://doi.org/10.1016/j.gca.2019.09.044

Heimsath, A. M., & Whipple, K. X. (2019). Strength matters: Resisting erosion across upland landscapes. *Earth Surface Processes and Landforms*, *44*, 1748–1754. https://doi.org/10.1002/esp.4609

Herman, F., Copeland, P., Avouac, J. P., Bollinger, L., Maheo, G., Le Fort, P., et al. (2010). Exhumation, crustal deformation, and thermal structure of the Nepal Himalaya derived from the inversion of thermochronological and thermobarometric data and modeling of the topography. *Journal of Geophysical Research: Solid Earth*, *115*(B6), B06407. https://doi.org/10.1029/2008jb006126

Hobiger, M., Wegler, U., Shiomi, K., & Nakahara, H. (2016). Coseismic and post-seismic velocity changes detected by passive image interferometry: Comparison of one great and five strong earthquakes in Japan. *Geophysical Journal International*, *205*(2), 1053–1073. https://doi.org/10.1093/gji/ggw066

Hodges, K. V., Hurtado, J. M., & Whipple, K. X. (2001). Southward extrusion of Tibetan crust and its effects on Himalayan tectonics. *Tectonics*, *20*(6), 799–809. https://doi.org/10.1029/2001tc001281

Hoek, E., & Brown, E. T. (1997). Practical estimates of rock mass strength. *International Journal of Rock Mechanics and Mining Sciences*, *34*(8), 1165–1186. https://doi.org/10.1016/S1365-1609(97)80069-X

Hoek, E., & Brown, E. T. (2019). The Hoek-Brown failure criterion and GSI – 2018 edition. *Journal of Rock Mechanics and Geotechnical Engineering*, *11*(3), 445–463. https://doi.org/10.1016/j.jrmge.2018.08.001

Hoek, E., Carranza-Torres, C., & Corkum, B. (2002). Hoek-Brown failure critierion – 2002 edition. *Proceedings of the Fifth North American Rock Mechanics Symposium* (Vol. 1, pp. 267–273).

Holbrook, W. S., Marcon, V., Bacon, A. R., Brantly, S. L., Carr, B. J., Flinchum, B. A., et al. (2019). Links between physical and chemical weathering inferred from a 65-m-deep borehole through Earth's critical zone. *Scientific Reports*, *9*, 4495. https://doi.org/10.1038/s41598-019-40819-9

Huang, D., Li, Y. Q., Song, X., Xu, Q., & Pei, X. J. (2019). Insights into the catastrophic Xinmo rock avalanche in Maoxian County, China: Combined effects of historical earthquakes and landslide amplification. *Engineering Geology*, *258*, 105158. https://doi.org/10.1016/j.enggeo.2019.105158

Jaky, J. (1944). The coefficient of earth pressure at rest. *Journal of the Society of Hungarian Architects and Engineers*, *1*, 355–358

Jeandet, L., Steer, P., Lague, D., & Davy, P. (2019). Coulomb mechanics and relief constraints explain landslide size distribution. *Geophysical Research Letters*, *46*, 4258–4266. https://doi.org/10.1029/2019gl082351

Kattel, D. B., Yao, T., Yang, K., Tian, L., Yang, G., & Joswiak, D. (2013). Temperature lapse rate in complex mountain terrain on the southern slope of the central Himalayas. *Theoretical and Applied Climatology*, *113*, 671–682. https://doi.org/10.1007/s00704-012-0816-6

Kump, R. L., Brantley, S., & Arthur, M. A. (2000). Chemical weathering, atmospheric CO2, and climate. *Annual Review of Earth and Planetary Sciences*, *28*, 611–667. https://doi.org/10.1146/annurev.earth.28.1.611

Le Fort, P. (1975). Himalayas: The collided range present knowledge of the continental arc. *American Journal of Science*, *275*(A), 1–44.

Lebedeva, M. I., & Brantley, S. L. (2013). Exploring geochemical controls on weathering and erosion of convex hillslopes: Beyond the empirical regolith production function. *Earth Surface Processes and Landforms*, *38*(15), 1793–1807. https://doi.org/10.1002/esp.3424

Leone, J. D., Holbrook, W. S., Riebe, C. S., Chorover, J., Ferré, T. P., Carr, B. J., & Callahan, R. P. (2020). Strong slope-aspect control of regolith thickness by bedrock foliation. *Earth Surface Processes and Landforms*, *45*(12), 2998–3010. https://doi.org/10.1002/esp.4947

Macfarlane, A. M. (1993). Chronology of the tectonic events in the crystalline core of the Himalaya, Langtang National park, Central Nepal. *Tectonics*, *12*(4), 1004–1025. https://doi.org/10.1029/93tc00916

Marc, O., Behling, R., Andermann, C., Turowski, J. M., Illien, L., Roessner, S., & Hovius, N. (2019). Long-term erosion of the Nepal Himalayas by bedrock landsliding: The role of monsoons, earthquakes, and giant landslides. *Earth Surface Dynamics*, *7*, 107–128. https://doi.org/10.5194/esurf-7-107-2019

Marc, O., Sens-Schonfelder, C., Illien, L., Meunier, P., Hobiger, M., Sawazaki, K., et al. (2021). Toward using seismic interferometry to quantify landscape mechanical variations after earthquakes. *Bulletin of the Seismological Society of America*, *111*(3), 1631–1649. https://doi.org/10.1785/0120200264

Mayne, P. W., & Kulhawy, F. H. (1982). K0-OCR relationship in soil. *Journal of the Soil Mechanics and Foundations Division*, *108*(6), 851–872. https://doi.org/10.1061/ajgeb6.0001306

Medwedeff, W. G., Clark, M. K., Zekkos, D., & West, A. J. (2020). Characteristic landslide distributions: An investigation of landscape controls on landslide size. *Earth and Planetary Science Letters*, *539*. https://doi.org/10.1016/j.epsl.2020.116203

Miller, D. J., & Dunne, T. (1996). Topographic perturbations of regional stresses and consequent bedrock fracturing. *Journal of Geophysical Research: Solid Earth*, *101*(B11), 25523–25536. https://doi.org/10.1029/96jb02531

Montgomery, D. R., & Brandon, M. T. (2002). Topographic controls on erosion rates in tectonically active mountain ranges. *Earth and Planetary Science Letters*, *201*(3–4), 481–489. https://doi.org/10.1016/s0012-821x(02)00725-2

Moon, S., Perron, J. T., Martel, S. J., Holbrook, W. S., & St. Clair, J. (2017). A model of three-dimensional topographic stresses with implications for bedrock fractures, surface processes, and landscape evolution. *Journal of Geophysical Research: Earth Surface*, *122*(4), 823–846. https://doi.org/10.1002/2016JF004155

Neely, A. B., DiBiase, R. A., Corbett, L. B., Bierman, P. R., & Caffee, M. W. (2019). Bedrock fracture density controls on hillslope erodibility in steep, rocky landscapes with patchy soil cover, southern California, USA. *Earth and Planetary Science Letters*, *522*, 186–197. https://doi.org/10.1016/j.epsl.2019.06.011

O'Neill, A., & Matsuoka, T. (2005). Dominant higher Surface-wave Modes and possible inversion pitfalls. *Journal of Environmental & Engineering Geophysics*, *10*, 185–201. https://doi.org/10.2113/JEEG10.2.185

Owen, L. A., & Benn, D. I. (2005). Equilibrium-line altitudes of the last glacial Maximum for the Himalaya and Tibet: An assessment and evaluation of results. *Quaternary International*, *138–139*, 55–78. https://doi.org/10.1016/j.quaint.2005.02.006

Park, C. B., Miller, R. D., & Xia, J. (1999a). Multichannel analysis of surface waves. *Geophysics*, *64*(3), 800–808. https://doi.org/10.1190/1.1444590

Park, C. B., Miller, R. D., & Xia, J. (1999b). Multimodal analysis of high frequency surface waves. *Proceedings of the 12th EEGS symposium on the application of geophysics to engineering and environmental problems*. https://doi.org/10.3997/2214-4609-pdb.202.1999_013

Parrish, R. R., & Hodges, V. (1996). Isotopic constraints on the age and provenance of the lesser and greater Himalayan sequences, Nepalese Himalaya. *GSA Bulletin*, *108*(7), 904–911. https://doi.org/10.1130/0016-7606(1996)108<0904:icotaa>2.3.co;2

Pasquet, S., & Bodet, L. (2017). SWIP: An integrated workflow for surface-wave dispersion inversion and profiling. *Geophysics*, *82*(6), WB47–WB61. https://doi.org/10.1190/geo2016-0625.1

Pedrazas, M. A., Hahm, W. J., Huang, M. H., Dralle, D., Nelson, M. D., Breunig, R. E., et al. (2021). The relationship between topography, bedrock weathering, and water storage across a sequence of ridges and valleys. *Journal of Geophysical Research: Earth Surface*, *126*(44), 217126. https://doi.org/10.1029/2020jf005848

Rempe, D. M., & Dietrich, W. E. (2014). A bottom-up control on fresh-bedrock topography under landscapes. *Proceedings of the National Academy of Sciences*, *111*(18), 6576–6581. https://doi.org/10.1073/pnas.1404763111

Riebe, C. S., Hahm, W. J., & Brantley, S. L. (2017). Controls on deep critical zone architecture: A historical review and four testable hypotheses. *Earth Surface Processes and Landforms*, *42*, 128–156. https://doi.org/10.1002/esp.4052

Riebe, C. S., Kirchner, J. W., & Finkel, R. C. (2004). Sharp decrease in long-term chemical weathering rates along an altitudinal transect. *Earth and Planetary Science Letters*, *218*, 421–434. https://doi.org/10.1016/s0012-821x(03)00673-3

Roback, K., Clark, M. K., West, A. J., Zekkos, D., Li, G., Gallen, S. F., et al. (2018). The size, distribution, and mobility of landslides caused by the 2015 Mw7.8 Gorkha earthquake, Nepal. *Geomorphology*, *301*, 121–138. https://doi.org/10.1016/j.geomorph.2017.01.030

Schickhoff, U. (2005). The upper timberline in the Himalayas, Hindu Kush and Karakorum: A Review of geographical and ecological aspects. In G. Broll, & B. Keplin (Eds.), *Mountain ecosystems* (pp. 275–354). Springer-Verlag.

Schmidt, K. M., & Montgomery, D. R. (1995). Limits to Relief. *Science*, *270*(5236), 617–620. https://doi.org/10.1126/science.270.5236.617

Selby, M. J. (1980). A rock mass strength classification for geomorphic purposes: With tests from Antarctica and New Zealand. *Zeitschrift für Geomorphologie*, *24*, 31–51. https://doi.org/10.1127/zfg/24/1984/31

Shearer, P. (2009). *Introduction to seismology*. Cambridge University Press. https://doi.org/10.1017/CBO9780511841552

Shelling, D., & Arita, K. (1991). Thrust tectonics, crustal shortening, and the structure of the far eastern Nepal Himalaya. *Tectonics*, *10*(5), 851–862. https://doi.org/10.1029/91TC01011

Shobe, C. M., Hancock, G. S., Eppes, M. C., & Small, E. E. (2017). Field evidence for the influence of weathering on rock erodibility and channel form in bedrock rivers. *Earth Surface Processes and Landforms*, *42*, 1997–2012. https://doi.org/10.1002/esp.4163

Shrestha, D., Singh, P., & Nakamura, K. (2012). Spatiotemporal variation of rainfall over the central Himalayan region revealed by TRMM Precipitation Radar. *Journal of Geophysical Research: Atmospheres*, *117*(D22). https://doi.org/10.1029/2012jd018140

Shrestha, D. B., & Shrestha, J. N. (1986). *Geological map of central NepalScale: 1:250,000*. Department of Mines and Geology.

Sklar, L. S., & Dietrich, W. E. (2001). Sediment and rock strength controls on river incision into bedrock. *Geology*, *29*(12), 1087–1090. https://doi.org/10.1130/0091-7613(2001)029<1087:sarsco>2.0.co;2

Slim, M., Perron, J. T., Martel, S. J., & Singha, K. (2015). Topographic stress and rock fracture: A two-dimensional numerical model for arbitrary topography and preliminary comparison with borehole observations. *Earth Surface Processes and Landforms*, *40*, 512–529. https://doi.org/10.1002/esp.3646

St. Clair, J., Moon, S., Holbrook, W. S., Perron, J. T., Riebe, C. S., Martel, S. J., et al. (2015). Geophysical imaging reveals topographic stress control of bedrock weathering. *Science*, *350*(6260), 534–538. https://doi.org/10.1126/science.aab2210

Stokoe, K. H., & Santamarina, J. C. (2000). Seismic-wave-based testing in geotechnical engineering. In *Proceedings International Conference on Geotechnical and Geological Engineering* (Vol. 1, pp. 1490–1536), Technomic Publishing, Lancaster, PA.

Sutcliffe, D., Yu, H., & Sloan, S. (2004). Lower bound solutions for bearing capacity of jointed rock. *Computers and Geotechnics*, *31*(1), 23–36. https://doi.org/10.1016/j.compgeo.2003.11.001

Takagi, R., Okada, T., Nakahara, H., Umino, N., & Hasegawa, A. (2012). Coseismic velocity change in and around the focal region of the 2008 Iwate-Miyagi Nairiku earthquake. *Journal of Geophysical Research: Solid Earth*, *117*(B6), B06315. https://doi.org/10.1029/2012jb009252

Townsend, K. F., Clark, M. K., & Zekkos, D. (2021). Profiles of near-surface rock mass strength across gradients in burial, erosion, and time. *Journal of Geophysical Research: Earth Surface*, *126*(4), e2020JF005694. https://doi.org/10.1029/2020jf005694

Townsend, K. F., Gallen, S., & Clark, M. K. (2020). Quantifying near-surface rock strength on a regional scale from hillslope stability models. *Journal of Geophysical Research: Earth Surface*, *125*(7), e2020JF005665. https://doi.org/10.1029/2020jf005665

Von Voigtlander, J., Clark, M. K., Zekkos, D., Greenwood, W. W., Anderson, S. P., Anderson, R. S., & Godt, J. W. (2018). Strong variation in weathering of layered rock maintains hillslope-scale strength under high precipitation. *Earth Surface Processes and Landforms*, *43*, 1183–1194. https://doi.org/10.1002/esp.4290

Wang, H. Y., & Wang, S. Y. (2015). A new method for estimating vs (30) from a shallow shear-wave velocity profile (depth <30 m). *Bulletin of the Seismological Society of America*, *105*(3), 1359–1370. https://doi.org/10.1785/0120140103

West, A. J., Galy, A., & Bickle, M. (2005). Tectonic and climate controls on silicate weathering. *Earth and Planetary Science Letters*, *235*(1–2), 211–228. https://doi.org/10.1016/j.epsl.2005.03.020

White, A. F., & Blum, A. E. (1995). Effect of climate on chemical weathering in watersheds. *Geochimica et Cosmochimica Acta*, *59*(9), 1729–1747. https://doi.org/10.1016/0016-7037(95)00078-e

Yoon, S., & Rix, G. J. (2009). Near-field effects on array-based surface wave methods with active sources. *Journal of Geotechnical and Geoenvironmental Engineering*, *135*(3), 399–406. https://doi.org/10.1061/(asce)1090-0241(2009)135:3(399)